

國立交通大學
光電工程研究所

碩士論文

非極性氮化鎵及氧化鋅之結構及光學特性之研究

Study on structural and optical properties of
non-polar GaN and ZnO

研究生：張家銘

指導教授：郭浩中 教授

盧廷昌 教授

中華民國九十七年六月

非極性氮化鎵及氧化鋅之結構及光學特性之研究

Study on structural and optical properties of non-polar GaN and ZnO

研究生: 張家銘
指導教授: 郭浩中 教授
 盧廷昌 教授

Student: Chia-Ming Chang
Advisor: Prof. Hao-Chung Kuo
 Prof. Tien-Chang Lu

國立交通大學

光電工程研究所

碩士論文

A Thesis

Submitted to Institute of Electro-Optical Engineering

College of Electrical Engineering

National Chiao Tung University

in Partial Fulfillment of the Requirements

for the Degree of

Master

In

Electro-Optical Engineering

July 2008

Hsinchu, Taiwan, Republic of China

非極性氮化鎵及氧化鋅之結構及光學特性之研究

研究生：張家銘

指導教授：郭浩中教授

盧廷昌教授

國立交通大學光電工程研究所碩士班

摘要

在我的論文裡，將我的研究分成兩個部份：第一個部份是利用熱退火處理來改善a平面的氮化鎵之材料品質，而第二部份是藉由插入a平面的氮化鎵來成長非極性的氧化鋅。改善成長於r平面藍寶石基板上的a平面氮化鎵是在氮氣的環境上利用熱退火於已長成的樣品上。在1000°C的a平面氮化鎵退火下，其表面的粗糙程度只有0.4奈米。X光繞射圖更証實了晶格品質的改善。由x光的Rocking curve實驗，對[0001]方向的氮化鎵而言，半高寬有隨著溫度從850到1100°C逐漸減少的現象。由穿遂式電子顯微鏡(Transmission Electron Microscope)的實驗結果指出在樣口經過1000°C的熱退火後，螺旋差排(Treading Dislocations)沿著[0001]方向的氮化鎵從每平方公分 5×10^{10} 減少到每平方公分 1.5×10^{10} ，而疊差的數量從每公分 8.7×10^5 減少到每公分 4.8×10^5 。室溫的光激發螢光光譜及對應的陰極激發光影像顯示在經過熱退火處理後，比起未經過熱退火處理的a平面氮化鎵而言，a平面氮化鎵的能帶邊緣發光強度有明顯的增加及有較大的發光區域，其中的主要原因是非輻射復合的中心數量的減少。

在實驗的第二部份，藉由插入a平面的氮化鎵當緩衝層，將非極性的氧化鋅層成長於r平面的藍寶石基板。由掃描式電子顯微鏡(Scanning Electron Microscope)的觀察，隨著成長溫度的增加，氧化鋅會從似小草狀的結構轉變成薄膜的結構。X光繞射圖及原子力顯微鏡更証實了成長的樣品具有非極性的方向及平整的表面。由光激發螢光光譜的結果，氧化鋅薄膜有最強的近能帶邊緣的發光波長在383奈米並抑制了深層能階的發光。變溫的光激發螢光光譜指出，隨著溫度的增加，中性施子束縛激子和中性受子束縛激子會漸漸的轉變成自由激子。藉由活化能的計算，當在高溫的時候，施子束縛的激子和受子束縛的激子的活化能分別對應於激子的束縛能和能量差介於受子束縛激子及施子束縛激子的能量，而在低溫的時候，分別對應於能量差介於施子束縛激子和自由激子及能量差介於受子束縛激子和施子受子對的能量。最後，非極性氧化鋅的薄膜有很大潛力可以運用在新穎的光電材料上。

Study on structural and optical properties of non-polar GaN and ZnO

Student : Chia-Ming Chang

Advisor: Prof. Hao-Chung Kuo

Prof. Tien-Chang Lu

Institute of Electro-Optical Engineering
National Chiao Tung University

Abstract

In this thesis, I divide my experiments into two parts: first is the crystal quality improvement of *a*-plane GaN by using thermal annealing process and second is growth of non-polar ZnO film via inserting *a*-plane GaN. The crystal quality improvement of *a*-plane GaN grown on *r*-plane sapphire was demonstrated by applying thermal annealing on as-grown samples in nitrogen ambient. The root mean square roughness of the surface was only 0.4 nm in the 1000 °C -annealed *a*-plane GaN. The crystal quality improvement was confirmed by the X-ray diffraction. Full width at half maximums of X-ray rocking curve for $[0001]_{\text{GaN}}$ was gradually decreased when the samples were treated with annealing temperatures from 850 to 1100°C. Transmission electron microscope resulted further indicated threading dislocations were decreased from $5 \times 10^{10} \text{ cm}^{-2}$ to $1.5 \times 10^{10} \text{ cm}^{-2}$ along $[0001]_{\text{GaN}}$ and stacking faults were decreased from $8.7 \times 10^5 \text{ cm}^{-1}$ to $4.8 \times 10^5 \text{ cm}^{-1}$ after the sample was annealed at 1000 °C. Room-temperature photoluminescence (PL) and corresponding cathodoluminescence image measurements showed band edge emission intensity for *a*-plane GaN with annealing was enhanced and revealed larger emission area compared to the regular *a*-plane GaN film, which was attributed to reduction of the non-radiative recombination centers.

In the second section, non-polar ZnO film was grown on *r*-plane sapphire via inserting *a*-plane GaN layer by using furnace. Scanning electron microscope revealed the morphologies of ZnO were transformed from grass-like structure to thin film with increasing the growth temperature. X-ray diffraction and atomic force microscope measurements confirmed that our sample possessed non-polar crystal orientation and smooth surface. PL results exhibited the film had strongest near band edge emission of 383 nm and quenching of deep level emission. Temperature-dependent PL indicated the neutral donor-bound excitons ($D^{\circ}X$) and accepted-bound excitons ($A^{\circ}X$) could gradually transit to free excitons (FX) with increasing temperature. The activation energies of $D^{\circ}X$ and $A^{\circ}X$ were close to exciton binding energy and the transition variation between $A^{\circ}X$ and $D^{\circ}X$ energy for high temperature, while those were close to difference between $D^{\circ}X$ and FX and between $A^{\circ}X$ and the acceptor-donor pair for low temperature. Non-polar ZnO films have great potential for applications of novel optoelectronic.

Acknowledgement

轉眼間，兩年的時間就這麼匆匆的過去，從在成功大學懵懂無知的我來到交通大學後，不論心態上或是處事上都有不少的成長；從實驗中，了解到現實生活中不論什麼情況，處事都要更加的嚴謹小心，對自己我變得更加積極的面對自己的人生。

在這兩年的碩士生涯裡，我慶幸的能有三位資深的教授來指導我：王興宗教授，郭浩中教授及盧廷昌教授。雖然碩士班只有短短兩年的學習，老師們仍是盡心盡力的指導，即使在忙碌的階段，老師們仍願抽空和我討論，糾正我的錯誤觀念。老師們對研究的熱忱及堅持，以及對學生的用心與指導，相信將來有一天誓必會成為世界一流的研究室。

特別感謝博士班柯宗憲學長這兩年來的親身指導，在研究上，是一位真誠、優秀、熱心、親切的學長，在生活上，更是一位不可或缺의良伴，除了研究上給予我相當多的指導外，待人處事上更是給予我經驗的分享，對我無微不至的照顧，感覺就像自己的親兄弟一樣，真是一位好的生活典範。記得在一次失敗的實驗後，當時的我心情相當的沮喪，一整個月都無心於實驗，就在我心情最低落的時候，宗憲學長及時給予我鼓勵，告訴我實驗的技巧與態度，讓我及時的振作並順利地度過這個難關。今天能夠順利的畢業，真的很感謝宗憲學長的幫助，少了你，我真的不知道何時才能夠畢業。同時也感謝其他的博士班學生，俊榮、輝閩、小朱、柏孝、士偉、明華、碩均…等，感謝你們這兩年的照應。

謝謝這兩年來在實驗室一起努力的戰友：柏源，駿哥，小恬恬，晁恩，子維，恕帆，承恩，士嘉，建達，小麥。士嘉，以前和你是同學時以為你是位敦厚老實的學生，經過了大學四年後，怎麼變得如此的嘴炮，果然人是會變的；承恩，和你聊天真是開心，總是有一堆好笑的事情可以講；恕帆、建達，雖然不常和你們講話，但和你們在同一個實驗仍然很開心；子維，最難忘的一件事就是和你一起打新生盃並拿下總冠軍，真的是

很過份，那有中鋒跑到外面來投三分球的。晁恩，你做實驗的態度真是讓我折服，細心程度和伯駿不相上下，也感謝你這兩年來的照應。柏源，同樣是湖人的球迷，一起看球總是充滿了樂趣，明年湖人一定會拿總冠軍的。小恬恬、小麥，謝謝你們這兩年來在實驗上的幫助，讓我可以順利完成我的實驗，也預祝小麥你也能早日的畢業；駿哥，你對實驗的堅持是眾所皆知的，很佩服你對實驗的熱忱，總是有用不完的精力，不過，你要改掉你的龜毛的習慣，這樣才能得到美女的親睜。和你們在一起，生活總是充滿了笑聲，總是有說不完的八卦，和你們一起出去吃飯是我一天最開心的時刻，一起聊天打屁，談論是非。又到時候說再見，在這裡，先預祝大家未來都能飛黃騰達。

碩一的學弟妹們：卓木，謝謝你在我自顧不暇的時候，幫我一起完成實驗，讓我減輕負擔許多，希望你在未來的一年裡實驗能夠順利的完成。還有就是尚樺、小柯、政暉、建綱、治凱、玫君、亭君、q q、生哥，預祝你們未來的一年裡，實驗能夠順利，明年都能夠順利的畢業。



還有，要感謝的就是在交大這兩年認識得朋友，飛鴨、芯芸、宜容、查、阿欽、芸芸、京橋、宛姍…等，有了你們讓我的碩士生活增添了許多的色彩，和你們一起出去玩總是有一堆做不完丟臉的事情。還有猩猩，你是大家的吉祥物，有你在，周遭總充滿歡樂，謝謝你帶給大家這麼多歡樂。

最後，感謝在交大認識的每一個人，預祝大家身體健康，事事順心。

Content

Abstract (in Chinese)	i
Abstract (in English)	ii
Acknowledgement	iii
Content	v
List of Figures	vii
Chapter 1 Introduction and Motivation	1
1-1 Introduction to opto-electronic material.....	1
1-2 Property of non-polar gallium nitride and zinc oxide.....	4
1-3 Review of thus far achievement and motivation	6
1-4 Overview	11
Chapter 2 Theoretical Background and Experiment Apparatus	12
2-1 Scanning electron microscope (SEM) and Transmission electron microscope (TEM)	12
2-2 Atomic force microscope (AFM)	18
2-3 X-ray diffraction (XRD)	19
2-4 Photoluminescence (PL)	21
2-5 Furnace.....	22
Chapter 3 Experiment Process, Results and Discussion	24
3-1 The effect of thermal annealing on non-polar <i>a</i> -plane GaN grown on <i>r</i> -plane sapphire	24
3-1-1 Samples preparation and growth.....	24
3-1-2 Structural and optical characterizations	25

3-1-3 Summary	31
3-2 Growth of non-polar ZnO nanostructures and films via using <i>a</i>-plane GaN buffer layer	40
3-2-1 Samples preparation and growth.....	41
3-2-2 Structural and optical characterizations	42
3-2-3 Summary	49
Chapter 4 Conclusion.....	57
Chapter 5 Future work and prospect	59
Reference	60



List of Figures

Fig. 1-1-1 Band bending resulted from QCSE in polar III-nitride quantum well with different thicknesses.....	3
Fig. 1-2-1 Schematic diagram of defects type in a-plane GaN (<i>J. Appl. Phys.</i> 94 , 942, 2003)...	5
Fig. 1-3-1 The PL spectrum of different polarization angles in m-plane GaN (a) and the comparison of PL intensity and the corresponding angle (b) (<i>Appl. Phys. Lett.</i> 71 , 1996, 1997).....	7
Fig. 1-3-2 Cross-section TEM of a-plane GaN grown on the r-plane sapphire substrate (a) and AFM image (b) (<i>Appl. Phys. Lett.</i> 81 , 469, 2002)	8
Fig. 1-3-3 The comparison of c-plane and a-plane AlGaIn/GaN quantum well with different thickness (<i>Appl. Phys. Lett.</i> 84 , 496, 2004).....	9
Fig. 1-3-4 AFM image of a-plane GaN without (a) and with (b) SiN _x layer on the surface (<i>Appl. Phys. Lett.</i> 89 , 041903, 2006).....	9
Fig. 2-1-1 Physical mechanism of electron beam occurring on the sample.....	13
Fig. 2-1-2 Ray diagram for viewing the image (a) and the diffraction pattern of the sample (b).	16
Fig. 2-2-1 The relation of the distance and interaction between the atoms.....	18
Fig. 2-3-1 Schematic viewing of X-ray diffractor setup	20
Fig. 2-4-1 The schematic diagram of photoluminescence setup	22
Fig. 3-1-1 The surface AFM image of a-plane GaN annealed at (a)850°C, (b)900°C, (c)950°C, (d)1000°C, (e)1050°C, and (f)1100°C.	32
Fig. 3-1-2 The SEM images of a-plane GaN annealed at (a)850°C, (b)900°C, (c)950°C, (d)1000°C, (e)1050°C, and (f)1100°C.	32
Fig. 3-1-3 θ -2 θ scan of the sample.	33
Fig. 3-1-4 FWHMs of X-ray rocking curves for the a-plane GaN along [0001] <i>c</i> and [1 $\bar{1}$ 00] <i>m</i> directions. The samples were annealed from 850 to 1100°C	34

Fig. 3-1-5 Bright field cross-section TEM images of <i>a</i> -plane GaN epilayer (a)(c)without/(b)(d)with annealing at 1000°C	35
Fig. 3-1-6 Plane-view TEM images of <i>a</i> -plane GaN epilayer (a) without/ (b) with annealing at 1000 °C. (c)HR-TEM of Atomic layer scanning and (d)Fourier-filtered image corresponding to the image in (c)	35
Fig. 3-1-7 The etching pits density of a-plane GaN without/with annealing at 1000°C	36
Fig. 3-1-8 The computations of lattice constant and mismatch under different annealing temperature.	36
Fig. 3-1-9 Room temperature PL spectra of the <i>a</i> -plane GaN annealed from 850 to 1000 °C.	37
Fig. 3-1-10 Room temperature PL spectra of the a-plane GaN annealed at different ambient gases	37
Fig. 3-1-11 Low temperature PL spectra of the a-plane GaN with/without annealing at 1000 °C.	38
Fig. 3-1-12 Room temperature PL spectra of the a-plane GaN annealed at 1000°C at different times.	38
Fig. 3-1-13 CL images show the surface emission of the <i>a</i> -plane GaN without/with annealing at 1000 °C	39
Fig. 3-2-1 Schematic drawing of growing a-plane ZnO on r-plane sapphire via inserting a-plane GaN as buffer layer.	50
Fig. 3-2-2 The surface SEM images of a-plane ZnO grown on r-plane sapphire via inserting a-plane GaN as buffer layer at the temperature of (a) 700°C 、(b) 800°C and (c) 900°C. (d)The cross-section SEM image indicates the thickness of the film is 3.394μm.....	51
Fig. 3-2-3 The surface SEM images of a-plane ZnO grown on r-plane sapphire via inserting a-plane GaN as buffer layer at the temperature of 900°C with growth period of (a) 6 hours, (b)7 hours, (c)8hours, and (d)9 hours.	51
Fig. 3-2-4 Schematic growth mechanism by using thermal vapor deposition on c-plane and a-plane substrate	52
Fig. 3-2-5 The surface AFM image of non-polar a-plane ZnO film. The RMS is 12.946nm. .	52
Fig. 3-2-6 (a) the θ -2 θ scan and (b) the rocking curve XRD pattern of the a-plane ZnO film. The $\varphi = 0^\circ$ (90°) represent that the (0001) direction of the ZnO is parallel	

(perpendicular) to the X-ray beam.	53
Fig. 3-2-7 Room temperature PL spectrum of ZnO nanograss, nanosprout, and film grown on r-plane sapphire via inserting a-plane GaN as buffer layer.	54
Fig. 3-2-8 Temperature-dependent PL analysis of a-plane ZnO. The neutral donor-bound exciton and acceptor-bound exciton were observed at low temperature.	54
Fig. 3-2-9 The calculation of the activation energy of donor-bound exciton and acceptor-bound exciton from the temperature-dependent PL.	56
Fig. 3-2-10 The fitting of the peak position in donor-bound exciton and acceptor-bound exciton with increasing temperature according to Varshni law.	56



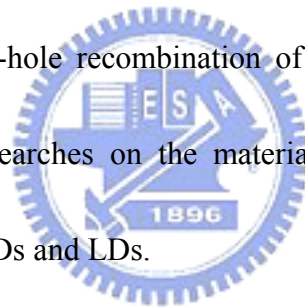
Chapter 1 Introduction and Motivation

1-1 Introduction to opto-electronic material

Nowadays, blue and UV light emitted diodes with efficiency, brightness, and longevity that are well in excess of those required for outdoor applications are highly expectable. With full of vital development of LEDs, LEDs have a variety of applications in the different field. Among the applications of them are indicator lights, signs, traffic lights, background lighting source of liquid crystal display, and lighting which requires emission in the visible part of the spectrum...etc.. Nevertheless, the current LEDs might have difficulties in the hard growth, low light efficiency, and large energy loss, which results in LEDs in the application of lighting are not good enough to replace the traditional fluorescent light. Potentially, further improvement in LEDs would be definitely required for the future life.

In recent years, the desire for blue and UV diode lasers and light emitting diodes has prompted enormous research efforts into II–VI and III–V wideband gap semiconductors. Among the well-known semiconductor materials employed in various technical applications, two unique positions are held by gallium nitride (GaN) and zinc oxide (ZnO) in the wide direct band gap semiconductor. In the material property, both GaN and ZnO have many similar aspects, such as material structure, lattice constant, energy band gap,... etc.. In the

difference of them, the remarkable property of ZnO better than GaN is exciton binding energy of 60 meV, which is only 30 meV for GaN. Owing to the larger exciton binding energy, more excitons exist in the room temperature, resulting in higher luminescence than GaN. Furthermore, ZnO can be grown at lower temperature on the cheaper substrate and lead to low cost of growth. However, because of more intrinsic defects, the hard growth of p-type ZnO to achieve the p-i-n junctions, and the degradation of material quality, the current commercial blue and UV LEDs are primitively composed of GaN. However, GaN-based LEDs still confront some problems of the luminescence, such as more defects in the material and low electron-hole recombination of *c*-direction growth. Therefore, it is worth making the further researches on the material of ZnO and GaN on purpose of possessing well-performed LEDs and LDs.



With the concern of growth technique, the material such GaN is grown on *c*-plane sapphire substrate in the field of the current commercial blue and green LEDs. The growth direction along *c*-axis could confront a problem that along the carrier flowing direction, because of asymmetric electric charge in the atom, built-in electric field exists in the GaN material. The causes of the built-in electric field exist two : one is different electric charges carried by group-III and group-V atoms and another is piezo-electric field resulted from the lattice mismatch between the material and the substrate, which is so-called quantum

confined stark effect (QCSE) [1][2]. The field leads to band bending and forces the carriers to the opposite side of the quantum well. The overlapping probability of the wave function taking place between electrons and holes would decrease, as weaken the lighting efficiency (Fig. 1-1-1).

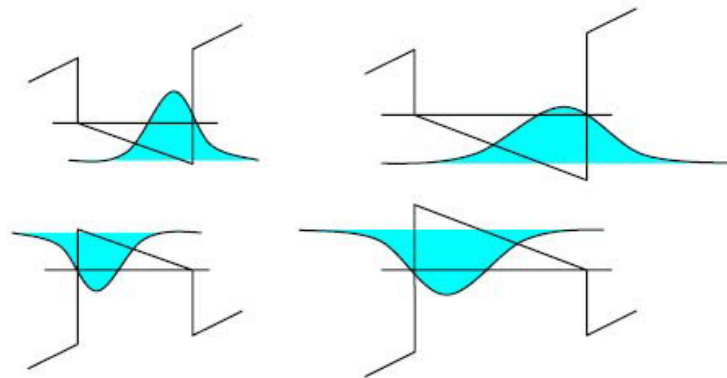


Fig. 1-1-1 Band bending resulted from QCSE in polar III-nitride quantum well with different thicknesses.

In the limit of the direction of material growth and polarization resulted from the hexagonal close-packed structure, the efficiency of the opto-electronic transformation is still not good enough. New outstanding materials or other directions of growth are definitely required to be investigated in detail. In the aspect of the non-polar plane, besides enhancement of opto-electronic transformation, the emission light from non-polar material is also in possession of the polarization properties, which has a great benefit in the application of opto-electronic device.

1-2 Property of non-polar gallium nitride and zinc oxide

The property of non-polar Gallium nitride

Gallium nitride is a III-V compound semiconductor with wide direct band gap of 3.42 eV in room temperature. Gallium Nitride is hexagonal close-packed structure with lattice constants of $a = 0.3189$ nm and $c = 0.5185$ nm. As the growth of GaN, the primitive growth direction is along $[0001]$, leading to high quality and low defect in the traditional (0001) -oriented GaN. However, on a -plane GaN, growth rate on c -axis direction is different to m -axis direction, and the growth rate on Ga face is 4 times faster than N face on c direction. It results in roughness surface and large dislocation. Typically, V-defect resulted from growing on the traditional c -plane GaN would change original type, which becomes \angle -defect. This defect type is aligned with $[0001]$ and the two inclined facets are $(10\bar{1}1)$ (Fig. 1-2-1). The growth direction along the $[0001]$ conduces the parallel stripes are on the non-polar surface, which is different to the (0001) -oriented surface.

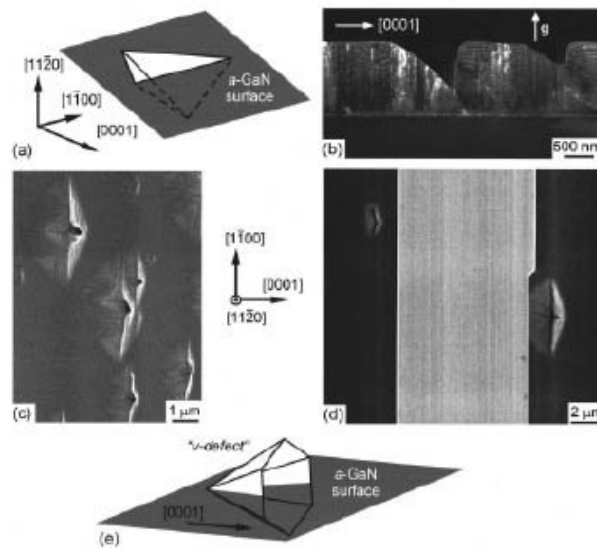


Fig. 1-2-1 Schematic diagram of defects type in a-plane GaN (*J. Appl. Phys.* **94**, 942, 2003)

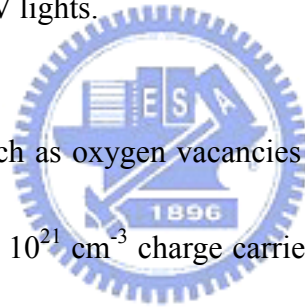
The property of zinc oxide



Zinc oxide is a II-VI compound semiconductor which unifies a couple of excellent material properties: a large direct band gap of 3.37 eV at room temperature, high transparency for visible light, chemical stability in terms of parasitic oxidation...etc.. Similar to GaN material, zinc oxide is hexagonal close-packed structure with lattice constant of $a = 0.3249$ nm and $c = 0.5209$ nm. Due to its large exciton binding energy of 60 meV, ZnO is a prime candidate for ultraviolet light emitting diodes and lasers suggesting even brighter light emission than the group-III nitrides [4]. Moreover, mixing Mg and Cd can result in ZnO as a tunable band gap between 3.0 and 4.0 eV, which could be used for fabrication of multi quantum wells in opto-electronic field [5]. Likewise, ZnO faces the

same problem of QCSE grown on polar (0001)-oriented plane

Because of C_{6v} symmetry, ZnO exhibits an optical anisotropy for transitions from three separate p-like valence bands (Γ_{9v} , Γ_{7v}^u , and Γ_{7v}^l in order of increasing transition energy [6]) to the s-like Γ_{7c} conduction band. Excitons related to the respective valence bands are referred to as A, B, and C excitons. The A and B transitions are allowed for light polarization E perpendicular to the c-axis ($E \perp c$), where E is the electric field, and the C transition is allowed for E parallel to the c axis ($E // c$). This anisotropy may provide various applications using polarized UV lights.



Intrinsic n-type defects such as oxygen vacancies (V_o) and zinc interstitials (Zn_i) exist in the ZnO material. Up to $2 \times 10^{21} \text{ cm}^{-3}$ charge carriers (n-type) can lead to hardly doping to become p-type ZnO [7]. In order to achieve the p-i-n ZnO junction, this important problem must be overcome. Despite all reports of p-type conductivity in ZnO using various growth methods and group-V dopant elements (N, P, As, Sb) [8], a reliable and reproducible high quality p-type conductivity is lacking.

1-3 Review of thus far achievement and motivation

In 1997, when commercial LEDs grown on the c-plane sapphire substrate were gradually in the development, Domen etc., in Fujitsu laboratory in Japan, grew m-plane

GaN on SiC by means of molecular beam epitaxy (MBE) and studied its optical properties and polarization. As the Fig. 1-3-1 shows, at the different polarization angles, m-plane GaN would produce discrepant photoluminescence spectra, which was due to, after valence band splitting, different energy band have different quantities of carrier transitions.

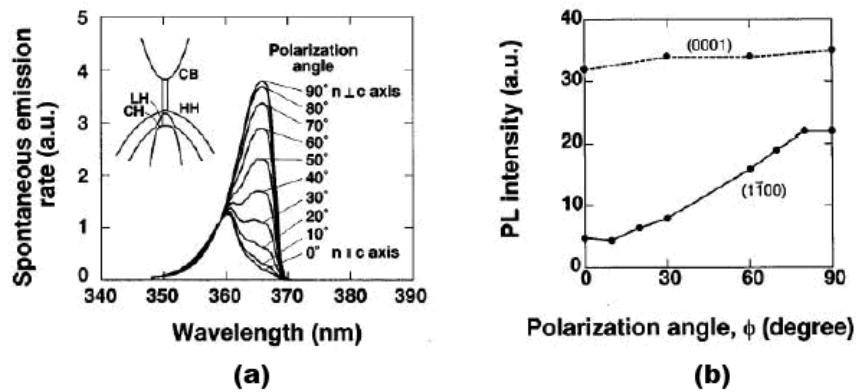


Fig. 1-3-1 The PL spectrum of different polarization angles in m-plane GaN (a) and the comparison of PL intensity and the corresponding angle (b) (*Appl. Phys. Lett.* 71, 1996, 1997)

In 2002, DenBaars and Speck *et al.*, at UCSB in America, began devoting themselves into development of non-polar materials. They first grew *a*-plane GaN film on *r*-plane sapphire substrate by using MOCVD, and analyzed quality by using TEM and AFM. It was observed that threading dislocations (TDs) of *a*-plane GaN was up to $2.6 \times 10^{10} \text{cm}^{-2}$. Normally, the TDs of *c*-plane GaN were only in the quantity of $10^7 \sim 10^8$. On the other hand, the result from AFM revealed roughness on the surface owing to a large number of dislocations passing through the material, which caused a lot of pits on the surface. As a

result of defects trapping radiative carrier, the quality of the film is difficult to hold high-efficiency radiation, even if the non-polar property theoretically has better electron-hole recombination rate than the *c*-plane.

In 2003, Nakamura performed the non-polar researches, which co-worked with Speck and DenBaars *et al.*. They grew about 50 μm *a*-plane GaN film by using HVPE. On further step of TEM analysis, the problems mentioned above still can not be overcome. The density of dislocation was up to $2 \times 10^{10} \text{cm}^{-2}$ (Fig. 1-3-2). DenBaars *et al.* compared a series of the quantum well thickness between *c*-plane and *a*-plane GaN/AlGaIn. In order to investigate best PL intensity (Fig. 1-3-3), they find conventional *c*-plane GaN/AlGaIn quantum well needs only 2.8nm, but 5.2 nm for *a*-plane. It is due to larger dislocations result in surface roughness, which caused non-smooth in the interface among the quantum well.

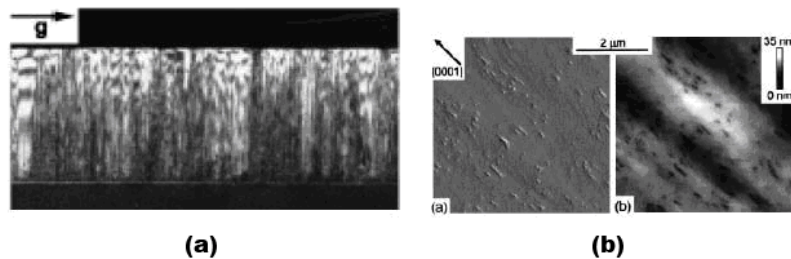


Fig. 1-3-2 Cross-section TEM of *a*-plane GaN grown on the *r*-plane sapphire substrate (a) and AFM image (b) (*Appl. Phys. Lett.* **81**, 469, 2002)

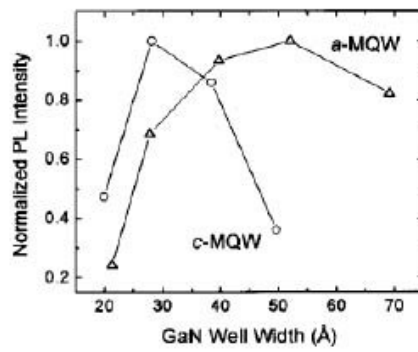


Fig. 1-3-3 The comparison of c-plane and a-plane AlGaIn/GaN quantum well with different thickness (*Appl. Phys. Lett.* **84**, 496, 2004)

In the limit of material growth, the development of *a*-plane material and device is extremely difficult. Using epitaxy lateral overgrowth (ELOG) might increase the difficulty of processing and raise the cost. Therefore, many groups dedicated to how to improve these non-polar materials. DenBaars *et al.* addressed inserting a SiN_x layer as nanomask in the growth process by using MOCVD [11]. After which growing *a*-plane GaN could decrease dislocation and stacking fault down to $9 \times 10^9 \text{ cm}^{-2}$ and $3 \times 10^5 \text{ cm}^{-1}$, respectively. AFM form Fig. 1-3-4 shows using SiN_x layer can improve surface roughness.

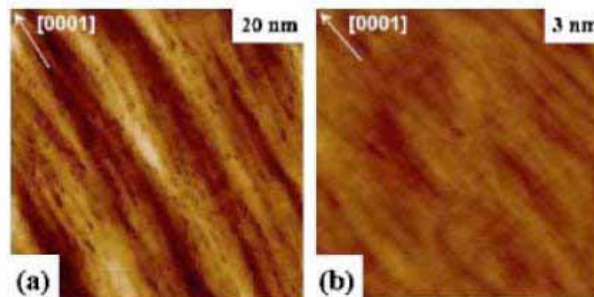


Fig. 1-3-4 AFM image of a-plane GaN without (a) and with (b) SiN_x layer on the surface

(*Appl. Phys. Lett.* **89**, 041903, 2006)

However, the quality of *a*-plane GaN grown on *r*-plane sapphire is usually not good enough for high performance devices due to the lattice mismatch and critical growth condition, which leads to a great number of threading dislocations (TDs) and stacking faults (SFs). Previously, there are several reports using thermal rapid annealing at high temperature to active Mg-doped GaN in a light emitting diode structure [12]. Afterward, it was reported that the annealing process could lead to the reduction of defects and the improvement of optical property of GaN [13] ~[15]. The annealing process is expected to be more convenient than epitaxially lateral over-growth technique and further improve the quality of *a*-plane GaN films briefly. By using a simple thermal annealing process, a smooth surface and less defect density in annealed *a*-plane GaN grown on *r*-plane sapphire could be beneficial to various optoelectronic device applications.

On the other hand, in recent years, ZnO are full of wide study. Although a fairly large body of literature exists on material structure, optic, device...etc. of ZnO, so many other niche researches of ZnO are not investigated, such as non-polar ZnO. Up to this point, there are few empirical studies of non-polar ZnO, which exist absolutely intriguing motivation.

1-4 Overview

The article is divided into three main sections. Section 1 is a description of background, which says why GaN and ZnO are selected to perform researches. Section 2 is the briefly introducing properties of non-polar GaN and ZnO. Section 3 is a review of the literature, addressing both empirical and theoretical aspects of non-polar GaN and ZnO, and motivation. This is followed by some background information on the ongoing research within which the present study was carried on and a statement of the specific research questions.



Chapter 2 outlines theoretical background and useful experiment apparatus to grow and measure the sample. Chapter 3 describes experiment results and discussions, which is separated into 2 parts. First is the effect of thermal annealing on *a*-plane GaN grown, and the other is growth of non-polar ZnO nanostructures and films using *a*-plane GaN buffer layer. Chapter 4 provides a conclusion of 2 part results in chapter 3. Chapter 5 is future work and prospect to have further studies.

Chapter 2 Theoretical Background and Experiment Apparatus

2-1 Scanning electron microscope (SEM) and Transmission electron microscope (TEM)

Physical mechanism of electron beam occurring on the sample can be summarized in the Fig. 2-1-1, which is absorption, emission, reflection, transmission, and even generation of light or X-ray emission. The secondary electrons emitted from the specimen and the incident electrons transmitting the specimen are interesting among those generated or inherent electrons for my measurement. Incident electrons can be focused, deflected, and accelerated by appropriate potentials. Their energy and angular distribution can be measured while sufficiently detected and counted. As the so-called nondestructive measurement, these electron beam measurements exhibit good morphology characterization. However, inasmuch as they are charged, they can cause samples charging, as may distort the measurement and lead to vague images.

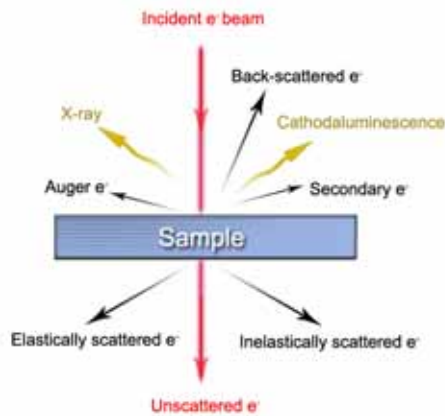


Fig. 2-1-1 Physical mechanism of electron beam occurring on the sample.

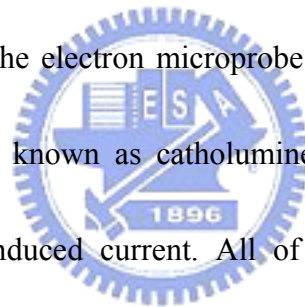
The basic structure of both SEM and TEM is illustrated above. The main spirit of the system is the electromagnetic optical system modulating the focus, by using magnetic lens, to form magnified image on the display. Right now, what I am going to discuss is the principle of useful electron beam characterization techniques used in my experiment:



1. Scanning Electron Microscope

An electron microscope utilizes an electron beam to produce a magnified image of the sample. There are three types of electron microscopes: scanning, transmission, and emission. In the scanning and transmission electron microscope, an electron beam incident on the sample produces image while in the field-emission microscope the specimen itself is the source of electrons. SEM is similar to light microscope with the different manner. SEM consists of an electron gun, a lens system, scanning coils, an electron collector, and a

display, so does the TEM. The electron energy is typically 10-30 KeV for most samples, but for insulating samples the energy can be as low as several hundred eV. The use of electrons has two main advantages over optical microscopes: much larger magnifications are possible since electron wavelengths are much smaller than photon wavelengths and the depth of the field is much larger. The image in an SEM is produced by scanning the sample with a focused electron beam and detecting the secondary or back-scattering electrons. Electrons and photons are emitted at each beam location and subsequently detected. Secondary electrons form the conventional SEM image, back-scattered electrons can also form an image, X-rays are used to in the electron microprobe as to lead to the Energy Dispersive Spectroscopy, emitted light is known as catholuminescence, and absorbed electrons are measured as electron-beam induced current. All of these signals can be detected and amplified synchronously via the scanning coil and then forming magnified images on the display.



2. Transmission Electron Microscope

Transmission electron microscope is the pre-eminent method for determining dislocation' and other crystallographic defects' character and for performing chemical and crystallographic analysis of micrometer and smaller precipitates and other microstructures.

With the similar structure and more powerful function compared with SEM, TEM offers the

in-depth perspective of specimen characterizations.

Any TEM is a complex assembly of magnetic lenses, several apertures, a sample holder and an image recording/viewing system (Fig. 2-1-2). The objective lens forms a diffraction pattern in the back focal plane with electrons scattered by the sample and combines them to generate an image in the image plane (1. intermediate image). Thus , diffraction pattern and image are simultaneously present in the TEM. It depends on the intermediate lens which of them appears in the plane of the second intermediate image and magnified by the projective lens on the viewing screen. Switching from real space (image) to reciprocal space (diffraction pattern) is easily achieved by changing the strength of the intermediate lens. In imaging mode, and objective aperture can be inserted in the back focal plane to select one or more beams that contribute to the final image (BF, DF, HRTEM). In selected area electron diffraction (SAED), an aperture in the plane of the first intermediate image defines the region of which the diffraction is obtained.

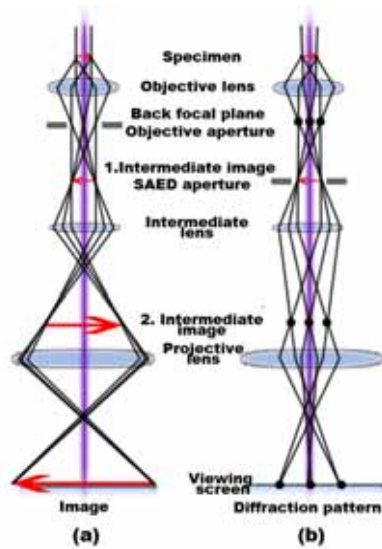


Fig. 2-1-2 Ray diagram for (a) viewing the image and (b) the diffraction pattern of the sample.

In the bright field (BF) mode of the TEM, an objective aperture is placed in the back focal plane of the objective lens which allows only the direct beam to pass. In this case, mass-thickness and diffraction contrast contribute to image formation: thick areas, areas in which heavy atoms are enriched, and crystalline areas appear with dark contrast. In spite of the useful information obtainable from BF images, it should be mentioned that the interpretation of contrast is often impeded since these phenomena occur simultaneously.

In dark field (DF) images, one or more diffracted beams are allowed to pass the objective aperture. The direct beam is blocked by the aperture. In contrast to the direct beam, the diffracted beam has interacted strongly with the specimen, and often very useful

information is present in DF images, e.g., about planar defects, stacking faults or particle size.

To obtain lattice images, a larger objective aperture has to be selected that allows many beams including the direct beam to pass. The image is formed by the interference of the diffracted beams with the direct beam (phase contrast). If the point resolution of the microscope is sufficiently high and a suitable sample oriented along a zone axis, then high-resolution TEM (HRTEM) images are obtained. In many cases, the atomic structure of the specimen can directly be investigated by HRTEM.

The incident parallel electron wave interacts elastically while passing through the specimen, and the resulting modulations of its phase and amplitude are present in the electron wave leaving the specimen. The wave here, the object exit wave $o(\mathbf{r})$, thus contains the information about the object structure. The objective lens performs

1. the Fourier transform (Fourier analysis) that creates the diffraction pattern of the object in the back focal plane and
2. the inverse Fourier transform (Fourier synthesis) that makes the interference of the diffracted beams back to a real space image in the image plane (lattice image).

2-2 Atomic force microscope (AFM)

AFM shows the surface properties of the sample by means of Van Der Waals force between the atoms. In the two atoms, one is the probe tip of the cantilever and the other is the surface of the desired sample. The interaction between them changes with the variation of the distance: the relation between interaction and distance is shown in Fig. 2-2-1. When an atom is close to another, the repulsive force among electrons is larger than the attractive force between the nucleus and electrons. Thus, the pure force of them is repulsive interaction. On the other hand, the pure force of them is attractive interaction in the opposite situation. In the AFM system, by means of the interaction of the tiny probe and the sample, the fluctuation of the cantilever may be made, recoding the shift of cantilever simultaneously. Finally, the surface property of the sample is clearly performed by images.

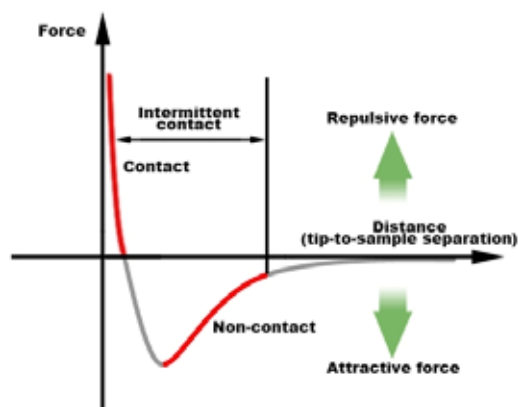


Fig. 2-2-1 The relation of the distance and interaction between the atoms

2-3 X-ray diffraction (XRD)

X-ray scattering techniques are famous of non-destructive analytical techniques which reveal information about the crystallographic structure, chemical composition, and physical properties of materials and thin films. These techniques are based on observing the scattered intensity of an x-ray beam hitting a sample as a function of incident and scattered angle, crystal orientation, and wavelength (Fig. 2-3-1).

A crystal lattice is a regular three-dimensional distribution (cubic, rhombic, etc.) of atoms in space. Atoms among the material are arranged into its own crystal lattice. A series of parallel planes formed in the crystal are separated from one another by a distance d , which varies according to the nature of the material. For any crystal, planes exist in a plenty of different orientations with its own specific d -spacing. In the diffraction, Bragg's law must be satisfied in any crystalline orientation, which is

$$2 d \sin \theta = n \lambda \qquad \text{Eq. 2-3-1}$$

where d is the spacing between the planes in the atomic lattice, θ is the angle between the incident ray and the scattering planes, n is an integer determined by the order given, and λ is the wavelength of X-ray. When a monochromatic X-ray beam with wavelength λ is projected onto a crystalline material at an angle θ , diffraction occurs only when the distance

travelled by the rays reflected from planes differs by a complete number n of wavelengths. Based on Bragg's Law, by varying the angle θ , the value of d -spacing must be satisfied at the corresponding angle. Plotting the angular positions and intensities of the resultant diffracted peaks of radiation produces a pattern, which is characteristic of the sample. If a mixture of different phases is present, the resultant diffractogram is formed by addition of the individual patterns. According to the principle of X-ray diffraction, a wealth of structural, physical and chemical information about the material investigated can be obtained from the diffraction patterns. Generally, XRD offers three types of scan: $\theta/2\theta$, rocking curve, and reciprocal space mapping. The wavelength of incident X-ray beam is 0.1542 nm of copper $K\alpha$ as the radiation source. The operating voltage and current are 40kv and 40mA respectively.

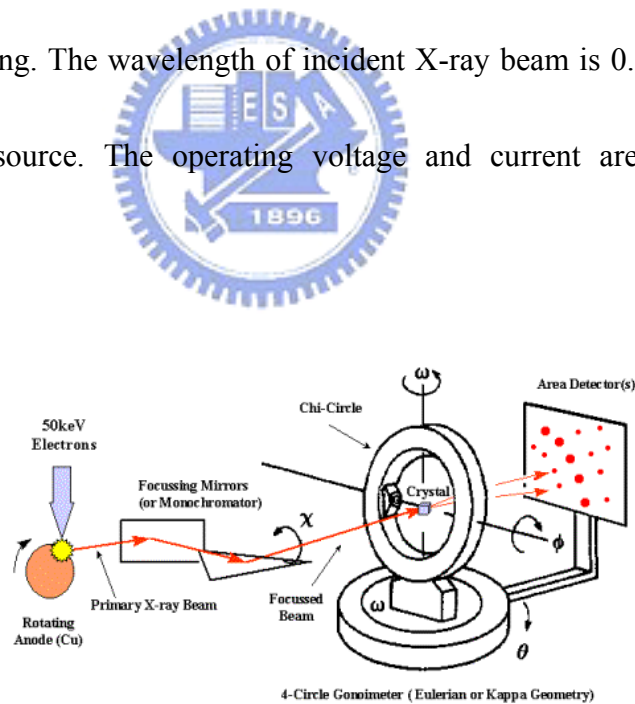


Fig. 2-3-1 Schematic viewing of X-ray diffractor setup

2-4 Photoluminescence (PL)

Photoluminescence, a powerful and breakless analysis technology, can reveal the band structure and the carrier transportation behaviors in a material. Moreover, the doping type, band gap, composition, etc. of the bulk material or the size, path of carrier transportation, lifetime, etc. of the nano-material will be shown in the photoluminescence spectrum.

Photoluminescence is a process in which a chemical compound absorbs photons (electromagnetic radiation), transitioning to a higher electronic energy state, and then radiates photons back out, returning to a lower energy state. The period between absorption and emission is extremely short, on the order of 10 nanoseconds. Light is directed on a sample, where it is absorbed and imparts excess energy into the material in a process called photo-excitation. The luminescence arising from photo-excitation is called photoluminescence (PL). The intensity and spectral content of the photoluminescence is a direct measurement of various important material properties. Fig. 2-4-1 shows the schematic setup of PL system with He-Cd laser operating at 25mW at the wavelength of 325nm.

Typically, the process of the luminescence consists of three steps, which is (1) excitation, (2) thermal equilibrium and (3) recombination. Through thermal equilibrium,

electron-hole pairs (e-h pairs) generated by incident light recombine and create photon. In the energy band gap, impurities and defects form a variety of energy levels, whose corresponding energy produces radiation through radiative recombination and absorption through non-radiative recombination.

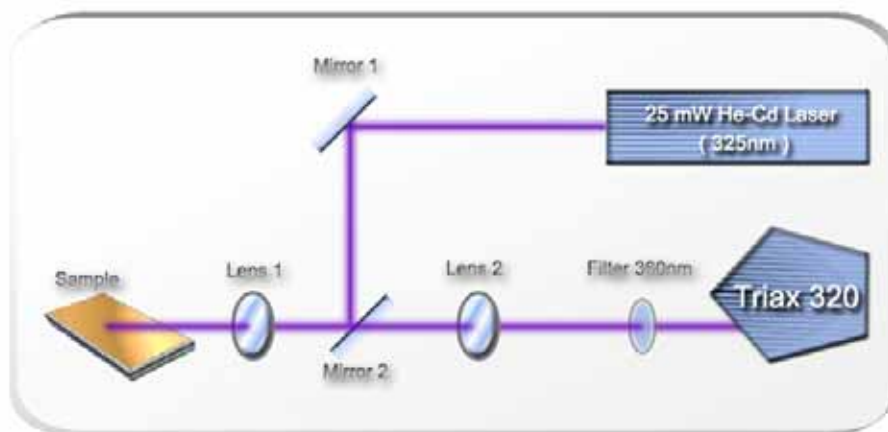


Fig. 2-4-1 The schematic diagram of photoluminescence setup

2-5 Furnace



This is a furnace with two-zone temperature controllers. And there are two kinds of gases provision. One is Nitrogen and the other is Oxygen. Attached to the end of the tube is

a mechanical pump, which can exert itself to exhaust the air inside the quartz tube to the extent of 0.01 Torr. In my experiments, two issues are performed. One is high-temperature annealing of non-polar *a*-plane GaN in order to improve material quality. The other is growth of non-polar ZnO on *r*-plane sapphire via inserting *a*-plane GaN.



Chapter 3 Experiment Process, Results and Discussion

3-1 The effect of thermal annealing on non-polar *a*-plane GaN grown on *r*-plane sapphire

The crystal quality improvement of *a*-plane GaN grown on *r*-plane sapphire was demonstrated by applying thermal annealing on as-grown samples in nitrogen ambient. The root mean square roughness of the 1000 °C -annealed *a*-plane GaN was only 0.4 nm measured by atomic force microscopy. Transmission electron microscopy results further indicated threading dislocations (TDs) were decreased from $5 \times 10^{10} \text{ cm}^{-2}$ to $1.5 \times 10^{10} \text{ cm}^{-2}$ along $[0001]_{\text{GaN}}$ and stacking faults (SFs) were decreased from $8.7 \times 10^5 \text{ cm}^{-1}$ to $4.8 \times 10^5 \text{ cm}^{-1}$ after the sample was annealed at 1000 °C. Room-temperature photoluminescence measurements showed band edge emission intensity was enhanced up to 10 folds compared to the regular *a*-plane GaN film. Furthermore, corresponding cathodoluminescence (CL) images revealed larger emission area for *a*-plane GaN with annealing than those without annealing, which was attributed to reduction of the non-radiative recombination centers.

3-1-1 Samples preparation and growth

A 30 nm-thick AlN nucleation layer was deposited on a 2-inch *r*-plane sapphire

substrate at 600 °C by using metal organic chemical deposition (MOCVD). Afterward, a 2 μm-thick GaN film was grown at 1080 °C. The V/III ratio was around 900 for the growth of bulk GaN with growth rate of 2 μm per hour. Afterwards, the as-grown samples were put into the thermal furnace and annealed in the temperature adjusted from 850 ~ 1100 °C for 4 hours in the nitrogen and oxygen ambient.

3-1-2 Structural and optical characterizations

The surface morphology and crystal quality of the samples were analyzed by AFM, SEM, and XRD. The TDs and SFs of the samples applied with 1000 °C annealing and without annealing were examined by using a TEM operated at 200 KV and etching pits density (EPD). Room and low temperature PL measurements were performed using a continue-wave 325 nm He-Cd laser operating at an excitation level of 25 mW to investigate the effect of annealing on luminescence enhancement of *a*-plane GaN. The spatially resolved CL mappings were obtained by SEM over the samples with the same viewing scale.

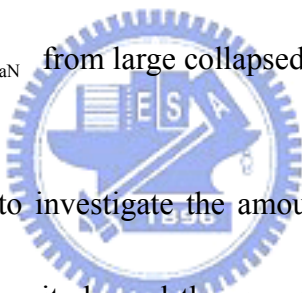
The root mean square (RMS) roughness of *a*-plane GaN annealed at different temperatures was analyzed by AFM as shown in Fig. 3-1-1. The RMS of these *a*-plane GaN samples confirmed that the surface was smoother when the annealing temperature was

raised from 850 to 1100 °C, which could be due to the repair of atoms near the surface. Fig. 3-1-1(d) shows the surface RMS of *a*-plane GaN annealed at 1000 °C is as low as 0.4 nm compared with the RMS value of 1.1 nm for the as-grown sample without annealing. The AFM results indicated the annealing process is benefit for surface morphology of *a*-plane GaN under suitable annealing conditions. However, surface morphologies of the annealed samples were gradually worse with increasing annealing temperature from 1000 to 1100°C, which could be due to that the temperature of 1100 °C is close to the thermal decomposition temperature of GaN [16].

The surface morphology was also analyzed by SEM (Fig. 3-1-2). When annealing temperature were raised from 850°C to 1000°C, the surface of *a*-plane GaN was as flat as as-grown *a*-plane GaN without annealing. But, it became rough at the annealing temperature of 1050°C and 1100°C. The collapse was clearly observed at 1100°C, which is in consistent with AFM results.

Single crystalline *a*-plane GaN was confirmed by X-ray θ - 2θ scan, which was located at the deflection angle of 57° (Fig. 3-1-3). The X-ray rocking curves along [0001] *c* and [$\bar{1}100$] *m* directions ($\Phi = 0^\circ$ and $\Phi = 90^\circ$, respectively) were measured for the samples with different annealing temperatures. The FWHMs of X-ray rocking curve measurements were plotted in Fig. 3-1-4. The FWHM of XRC for [0001]_{GaN} was gradually decreased

when the samples were treated with annealing temperatures from 850 to 1100°C, whereas the FWHM of rocking curve for $[\bar{1}\bar{1}00]_{\text{GaN}}$ was gradually increased for the samples with annealing temperature from 850 to 1050 °C. This result implied that the crystal orientation in the samples with annealing was getting uniform along $[0001]_{\text{GaN}}$ but more dispersive along $[\bar{1}\bar{1}00]_{\text{GaN}}$ [17], which could result in generation of the different strains along $[0001]_{\text{GaN}}$ and $[\bar{1}\bar{1}00]_{\text{GaN}}$ respectively. In addition, once the annealing temperature was increased up to 1100 °C, which was close to the thermal decomposition temperature, the FWHM of rocking curve for $[\bar{1}\bar{1}00]_{\text{GaN}}$ was dropped abruptly due to the stress release and crystal relaxation along $[\bar{1}\bar{1}00]_{\text{GaN}}$ from large collapsed portions of the sample.



TEM was further applied to investigate the amount of TDs and SFs in *a*-plane GaN sample annealed at 1000°C since it showed the smoothest surface which was suitable for further device fabrication and process. The defect distributions along both *c* and *m* directions and planar defects of our *a*-plane GaN films were investigated. Fig. 3-1-5 shows the bright-field cross-sectional TEM images and Fig. 3-1-6 shows the plane-view TEM images for our samples. Fig. 3-1-5 (a) and (b) are TEM images observed along $[0001]_{\text{GaN}}$ and Fig. 3-1-5 (c) and (d) are along $[\bar{1}\bar{1}00]_{\text{GaN}}$. Fig. 3-1-5(a), and (c) in the left column are the images for the sample without annealing and Fig. 3-1-5(b), and (d) are for the sample annealed at 1000 °C. The TD density along $[0001]_{\text{GaN}}$ for the sample without annealing

calculated by Fig. 3-1-5 (a) was $5.1 \times 10^{10} \text{ cm}^{-2}$. After annealing at $1000 \text{ }^\circ\text{C}$, the TD density of the sample along $[0001]_{\text{GaN}}$ shows in Fig. 3-1-5(b) was reduced down to $1.5 \times 10^{10} \text{ cm}^{-2}$. On the other hand, the TD density along $[\bar{1}\bar{1}00]_{\text{GaN}}$ was decreased from $6.8 \times 10^{10} \text{ cm}^{-2}$ to $4.3 \times 10^{10} \text{ cm}^{-2}$ calculated from Fig. 3-1-5 (c) and (d). Another way to investigate the dislocation density was using etching pits density. Fig. 3-1-7 shows the TD density of the sample without annealing is $1.5 \times 10^8 \text{ cm}^{-2}$, which is more than the value of $0.85 \times 10^8 \text{ cm}^{-2}$ with annealing.

Annealing is a useful technique that can activate disordered atoms to move to steady positions in the crystal and further repair the crystal lattice [18], which could be main reasons for the reduction of TDs. Except for the difference of lattice constants between a -plane GaN and r -plane sapphire, the thermal expansion coefficients are also different in c and m directions. We calculated the lattice constants a and c for both GaN and sapphire at room temperature of 1000°C by using the Eq. 3-1-1,

$$\frac{\Delta l}{l} = C_{th} \times (T - T_0) \quad \text{Eq. 3-1-1}$$

, where l is the initial lattice length, Δl is the difference of length when temperature was increased from T_0 to T , and C_{th} is the thermal expansion coefficient of materials.

Table 3-1-1

	Lattice constant (Å)		Thermal expansion coefficient ($10^{-6}/\text{K}$)	
	GaN	Sap.	GaN	Sap.
c	5.185	12.991	3.17	8.5
a	3.189	4.758	5.59	7.5

According to the useful parameters in table 3-1-1, we obtained two lattice mismatches along $[0001]_{\text{GaN}}$ and $[\bar{1}\bar{1}00]_{\text{GaN}}$ of *a*-plane GaN between *a*-plane GaN and *r*-plane sapphire [17].

The calculation results indicated that the lattice mismatch at high temperature was decreased from 1.1% to 0.6% along $[0001]_{\text{GaN}}$ while it was decreased from 16.1% to only 15.9% along $[\bar{1}\bar{1}00]_{\text{GaN}}$ (Fig. 3-1-8). This could conduce to explain more reduction of TDs along $[0001]_{\text{GaN}}$ than that along $[\bar{1}\bar{1}00]_{\text{GaN}}$.

On the other hand, Fig. 3-1-6 (c) shows atomic layer scanning and Fourier-filtered image is analyzed in Fig. 3-1-6 (d). Plenty SFs were observed in Fig. 3-1-6, which were generally observed on the *c*-plane sidewalls and generated from three-dimensional islands during the initial stages of the high temperature growth. In Fig. 3-1-6, the SFs of the sample annealed at 1000°C decreased from $8.7 \times 10^5 \text{ cm}^{-1}$ down to $4.8 \times 10^5 \text{ cm}^{-1}$, which probably attributed to the contribution of thermal annealing energy facilitating relocation of more atoms into stable positions.

Fig. 3-1-9 shows the room temperature PL of the annealed samples with different annealing temperatures. These spectra revealed the intensity of band-edge emission was enhanced for the annealed *a*-plane GaN [19][20]. In our experiments, the intensity of band-edge emission for *a*-plane GaN gradually increased with increasing annealing temperature from 850 to 1000°C and the deep level emission around 450 nm of the *a*-plane GaN, which was attributed to nitrogen vacancies [35], after annealing was obviously suppressed. The peak emission intensity of the sample with annealing at 1000°C was enhanced up to about 10 folds compared to the as-grown *a*-plane GaN film. The enhancement of PL intensity could be attributed to fewer defects and non-radiative centers trapping the photo-generated carriers after the sample was annealed, which is in accordance with the TEM results. The ambient oxygen gas was also performed. Fig. 3-1-10 shows annealing at O₂ ambient is worse, which is due to defects generated from gallium oxide [22]. The enhancement of PL intensity with annealing was also confirmed in low temperature (Fig. 3-1-11). The variation of annealing time was performed in Fig. 3-1-12. 4-hour annealing of *a*-plane GaN showed the best PL intensity, which is corresponding to the least defects. Fig. 3-1-13 shows CL emission images for samples with and without annealing at 1000 °C using optical filters at corresponding peak emission wavelength. The samples with annealing exhibited many relatively larger and more uniform luminescence patterns, indicating a higher crystal quality of the *a*-plane GaN. On the contrary, the sample without

annealing showed few and small luminescence patterns, demonstrating a worse crystal quality of the *a*-plane GaN, which was consistent with room temperature PL results. As a result, the stronger PL spectra and more uniform CL images could evidence that annealing process on *a*-plane GaN could really improve the crystal quality.

3-1-3 Summary

In summary, we have demonstrated that thermal annealing process was effective for improving the crystal quality and optical characteristics of *a*-plane GaN grown on *r*-plane sapphire. The AFM indicated *a*-plane GaN annealed at 1000 °C has RMS of 0.4 nm. TEM results further indicated threading dislocations was decreased from $5 \times 10^{10} \text{ cm}^{-2}$ to $1.5 \times 10^{10} \text{ cm}^{-2}$ along $[0001]_{\text{GaN}}$ and stacking faults was decreased from $8.7 \times 10^5 \text{ cm}^{-1}$ to $4.8 \times 10^5 \text{ cm}^{-1}$ after annealing at 1000 °C. Furthermore, room temperature PL measurements and corresponding CL images show *a*-plane GaN annealed at 1000 °C possesses stronger band edge emission intensity and larger emission area than that without annealing. By using a simple thermal annealing process, a smooth surface and less defect density in annealed *a*-plane GaN grown on *r*-plane sapphire could be beneficial to various optoelectronic device applications.

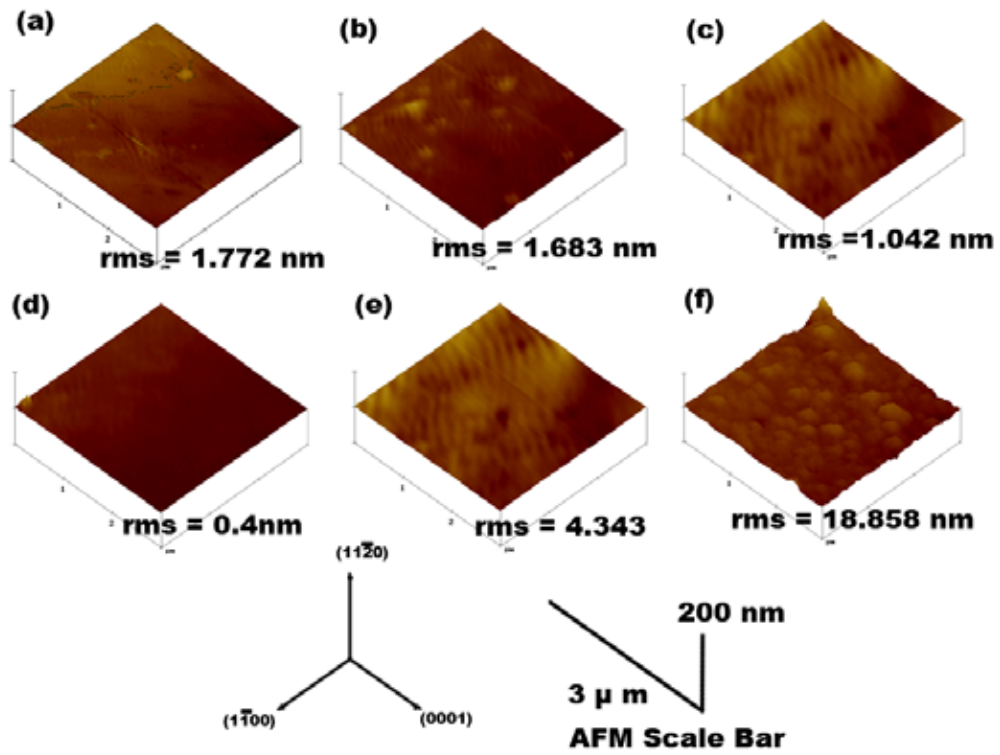


Fig. 3-1-1 The surface AFM image of *a*-plane GaN annealed at (a)850°C, (b)900°C, (c)950°C, (d)1000°C, (e)1050°C, and (f)1100°C.

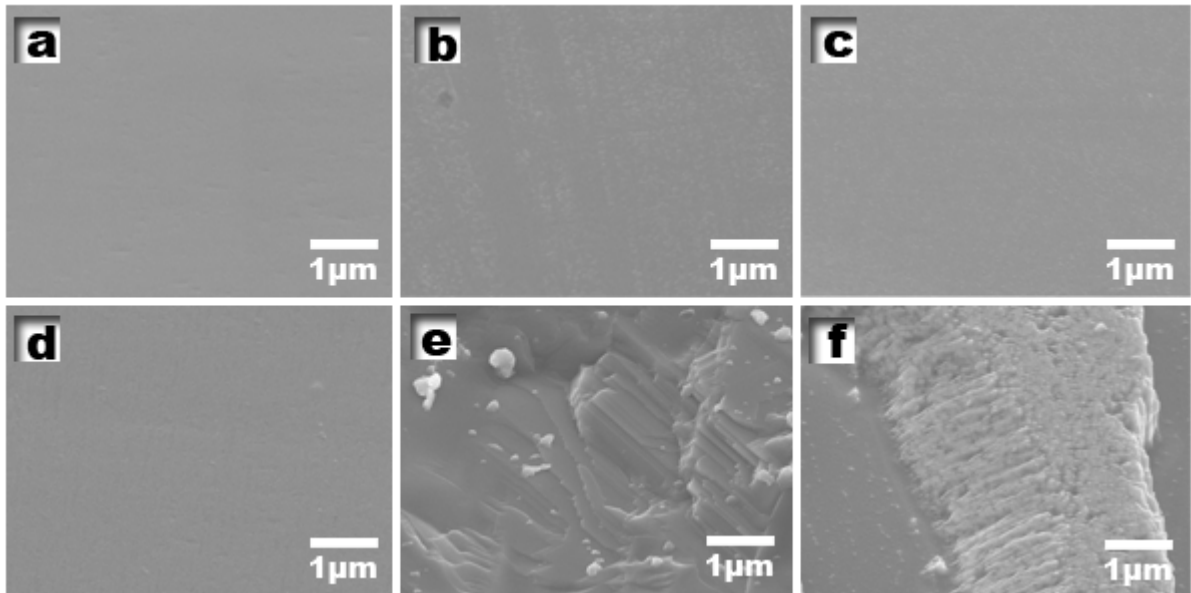


Fig. 3-1-2 The SEM images of *a*-plane GaN annealed at (a)850°C, (b)900°C, (c)950°C, (d)1000°C, (e)1050°C, and (f)1100°C.

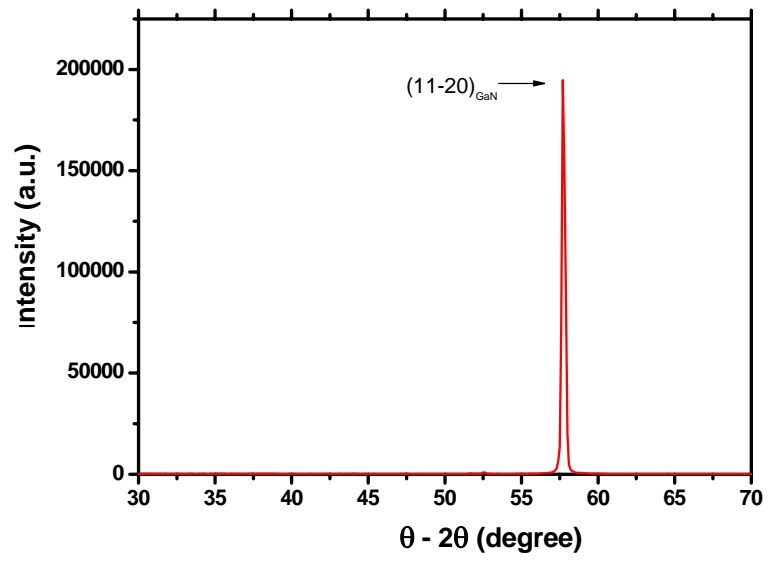


Fig. 3-1-3 θ - 2θ scan of the non-polar *a*-plane GaN.



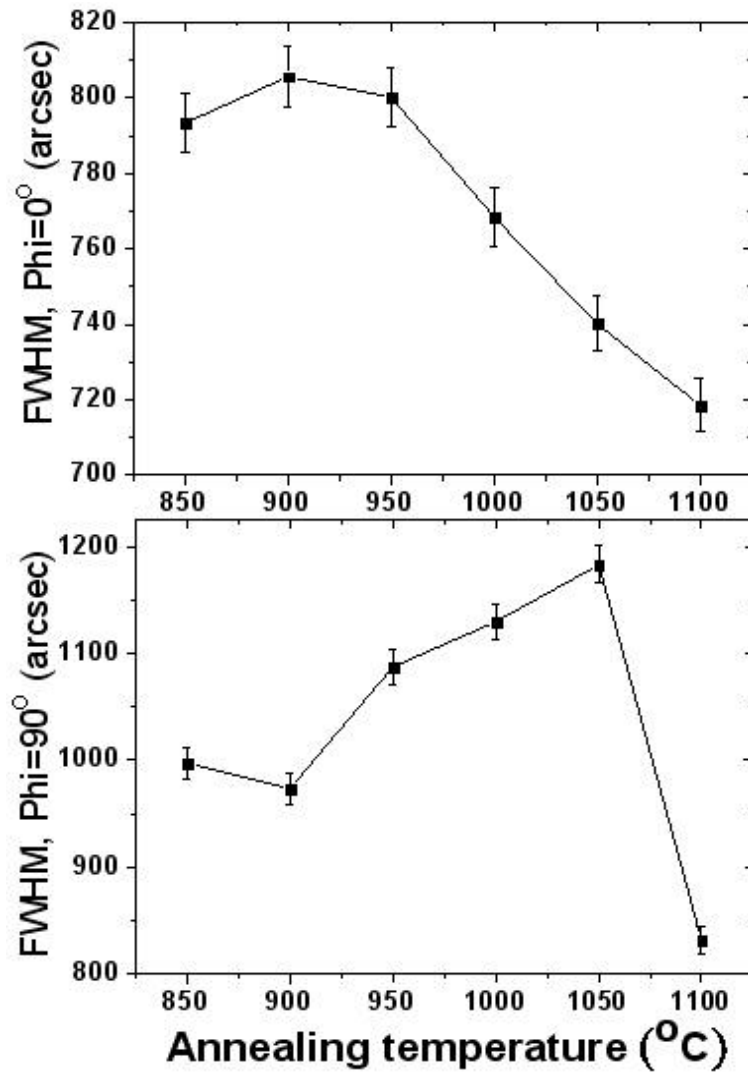


Fig. 3-1-4 FWHMs of X-ray rocking curves for the *a*-plane GaN along [0001] *c* (Phi=0°) and $[\bar{1}\bar{1}00]$ *m* (Phi=90°) directions. The samples were annealed from 850 to 1100°C.

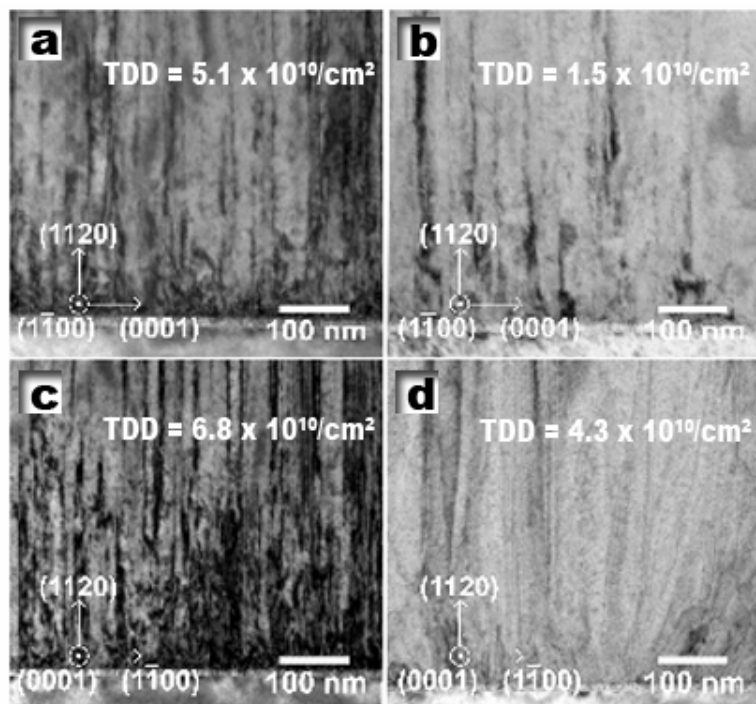


Fig. 3-1-5 Bright field cross-section TEM images of *a*-plane GaN epilayer (a)(c)without/(b)(d)with annealing at 1000 °C.

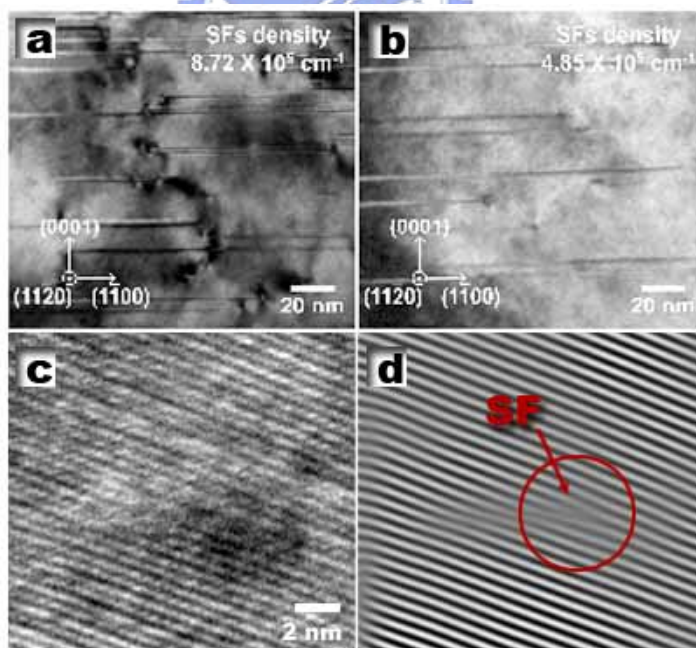


Fig. 3-1-6 Plane-view TEM images of *a*-plane GaN epilayer (a) without/ (b) with annealing at 1000 °C. (c)HR-TEM of Atomic layer scanning and (d)Fourier-filtered image corresponding to the image in (c)

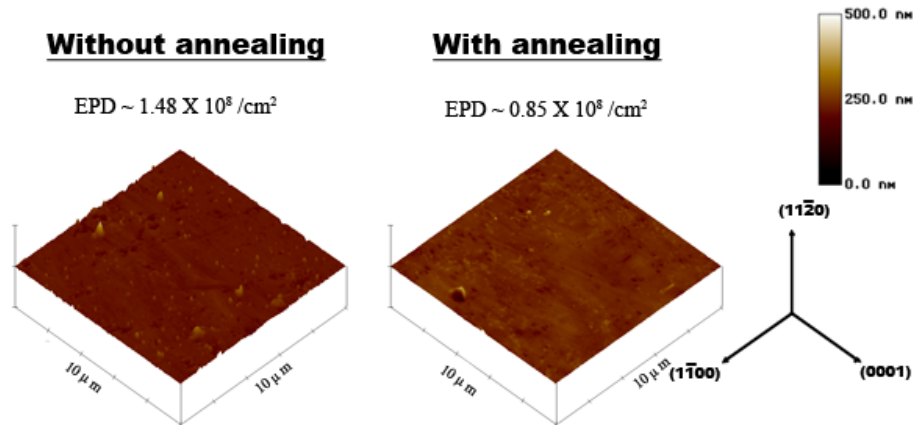


Fig. 3-1-7 The etching pits density of *a*-plane GaN without/with annealing at 1000°C

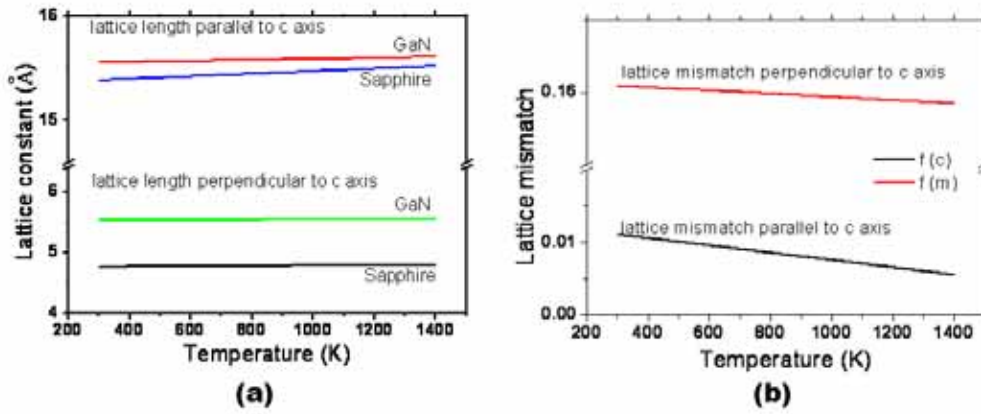


Fig. 3-1-8 (a) the computations of lattice constant and (b) lattice mismatch under different temperatures.

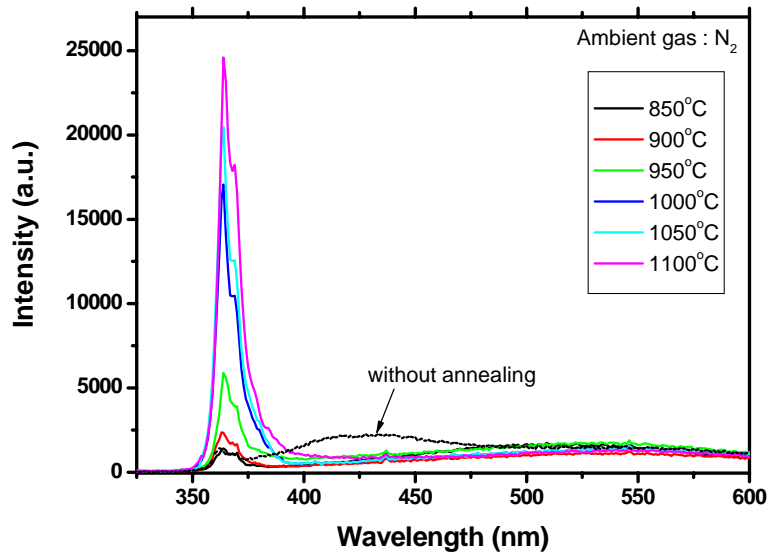


Fig. 3-1-9 Room temperature PL spectra of the *a*-plane GaN annealed from 850 to 1000 °C .

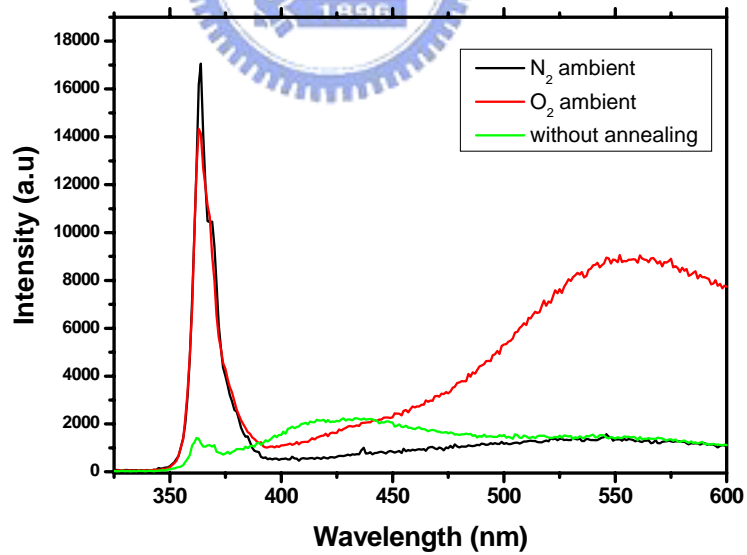


Fig. 3-1-10 Room temperature PL spectra of the *a*-plane GaN annealed at different ambient gases

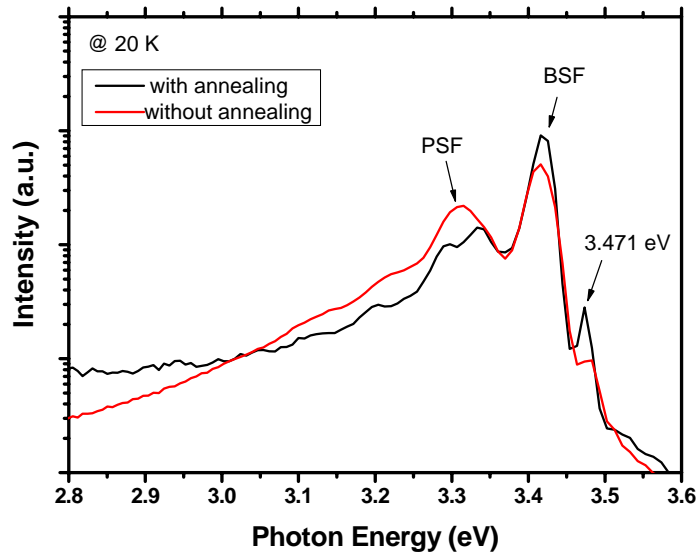


Fig. 3-1-11 Low temperature PL spectra of the *a*-plane GaN with/without annealing at 1000°C. It implies near band edge emission at 3.471eV was enhanced after thermal annealing process.

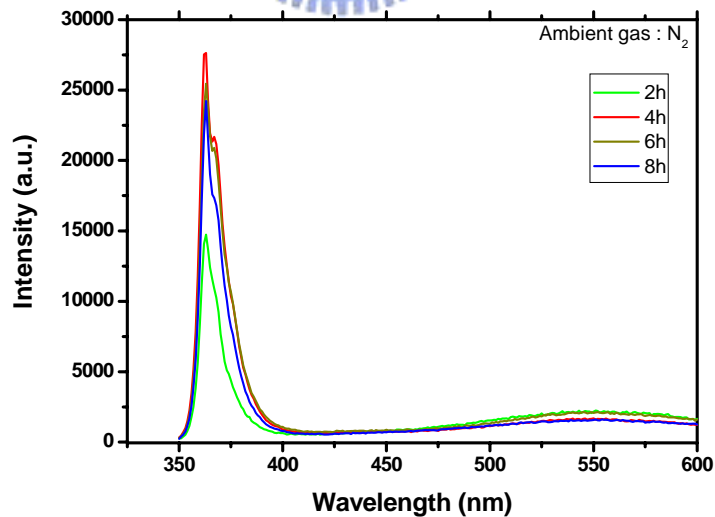


Fig. 3-1-12 Room temperature PL spectra of the *a*-plane GaN annealed at 1000°C at different times.

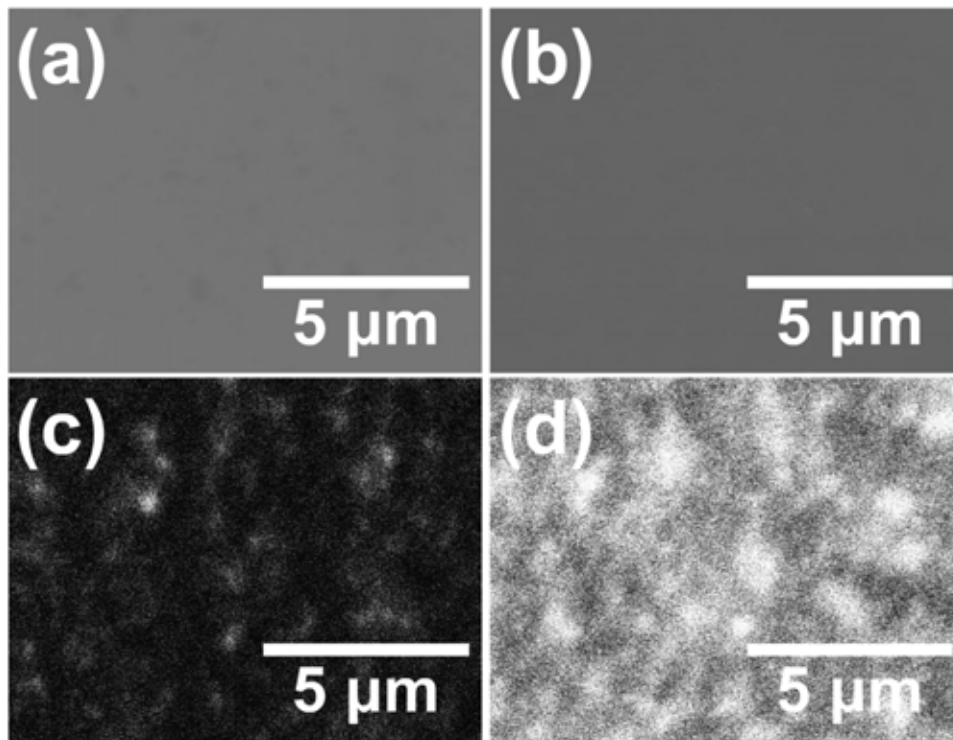
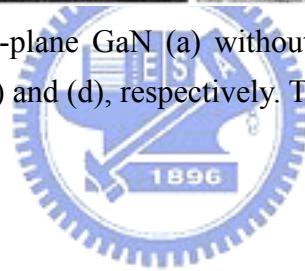


Fig. 3-1-13 SEM images of α -plane GaN (a) without/(b) with annealing at 1000 °C and corresponding CL images in (c) and (d), respectively. The emission wavelength is 362 nm.



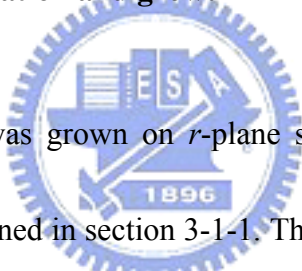
3-2 Growth of non-polar ZnO nanostructures and films via using *a*-plane GaN buffer layer

ZnO has a wurtzite structure, with the (0001) planes being Zn terminated and its (000 $\bar{1}$) being O terminated. ZnO has a partial ionic character, which results in a partial and opposite charge on the (0001) and (000 $\bar{1}$) planes. Thus there is a net dipole moment when the crystal is terminated by the basal plane, and it causes the higher surface energy [23]. The (1 $\bar{1}$ 20) and (1 $\bar{1}$ 00) planes are non-polar and have a lower surface energy compared to the basal plane. This results in a high growth rate along the *c* axis and a pillar-like morphology grown on *c*-plane sapphire. For the (1 $\bar{1}$ 20) ZnO films grown on *r*-plane sapphire, the *c* axis is in the plane of the film, which results in the absence of a pillar-like structure.

In this study, non-polar ZnO film was grown on *r*-plane sapphire via inserting *a*-plane GaN layer by using thermal vapor deposition. Scanning electron microscope (SEM) revealed the morphologies of ZnO were transformed from grass-like structure to films with increasing the growth temperature. X-ray diffraction (XRD) and atomic force microscope (AFM) measurement confirmed that our sample possessed non-polar crystal orientation and smooth surface. Photoluminescence (PL) results exhibited the near band edge emission

wavelength of 383 nm and deep level emission in the green band. Temperature-dependent PL indicated the neutral donor-bound exciton ($D^{\circ}X$) and accepted-bound exciton ($A^{\circ}X$) could gradually transit to free exciton (FX) with increasing temperature. The activation energies of $D^{\circ}X$ and $A^{\circ}X$ were close to exciton binding energy and the transition variation between $A^{\circ}X$ and $D^{\circ}X$ energy for high temperature, while those was close to difference between $D^{\circ}X$ and FX and between $A^{\circ}X$ and the donor-acceptor pair (DAP) energy for low temperature.

3-2-1 Samples preparation and growth



At first 2 μ m GaN film was grown on *r*-plane sapphire using MOCVD. The detail growth parameters can be obtained in section 3-1-1. The sample was placed in the two-zone furnace for growth of ZnO film. Oxygen flowing at the rate of 100 sccm was the carrier gas. 1g metal zinc was positioned upstream and the substrate was placed downstream. The source vapor was transported by carrier gas and condensed on the substrates. The temperatures ramped up to 900 $^{\circ}$ C for sources and up to 700 $^{\circ}$ C~900 $^{\circ}$ C for substrates. The typical reaction time was 6 hours for film and the growth pressure was around 0.1 torr. The schematic representation was shown in Fig. 3-2-1.

3-2-2 Structural and optical characterizations

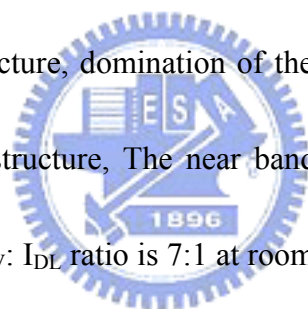
The morphology of the samples was investigated by SEM and AFM. Fig. 3-2-2 (a)~(c) show the SEM images of non-polar ZnO at growth temperatures of 700 °C, 800 °C, and 900 °C, which reveal nanograss, nanosprout, and film structures, respectively. These SEM images indicated the ZnO structures were transformed from grass-like structure to the film with increasing the growth temperature. Fig. 3-2-3 demonstrates the best growth period of non-polar ZnO film was 8 hours owing to flattest surface morphology. In the past, some groups investigated the ZnO growth on the *c*-plane substrate by using thermal furnace [24]. However, the nano wires were often found during the experiments, which is because growth rate of *c*- direction is faster than that of *a*- or *m*- direction. Fig. 3-2-4 shows, if *c* axis is lying on the surface such as *a*-plane or *m*-plane substrate, the film may be achieved during the growth owing to lower formation energy. Fig. 3-2-2 (d) shows the cross-section SEM image revealed the ZnO film could be deposited up to 3.39μm. Furthermore, AFM is used to analyze the surface morphology of ZnO film. The surface of the ZnO film has nanoscale stripes running along a specific direction (Fig. 3-2-5). The direction parallel to the stripes is determined to be [0001] direction of ZnO. It is because the growth rate along *c*-direction was faster than *m*-direction, which is the same morphology observed in the *a*-plane GaN grown on the *r*-plane sapphire substrate. In addition, RMS of non-polar ZnO is 12.9 nm.

Fig. 3-2-6 (a) shows a θ - 2θ scan X-ray patterns of ZnO film which indicated that the film have $(1\bar{1}\bar{2}0)$ orientation, but $(\bar{1}\bar{1}01)$ and $(\bar{1}\bar{1}02)$ reflections were also observed in the log scale, which confirmed our ZnO film was polycrystalline. Crystalline quality of the ZnO film was addressed by X-ray rocking curve (XRC). In order to measure the in-plane mosaic, XRC of the ZnO on-axis $(1\bar{1}\bar{2}0)$ reflection were measured. The on-axis XRCs were acquired with different ϕ angles ($\phi=0^\circ$ and 90°), where the $\phi=0^\circ$ (90°) represent that the $[0001]$ direction of the ZnO is parallel (perpendicular) to the X-ray beam. The FWHMs of XRC in Fig. 3-2-6 (b) for the non-polar ZnO film were about 915 arcsec with $\phi=0^\circ$ and 1180 arcsec with $\phi=90^\circ$. The difference in FWHMs with the ϕ angles in on-axis omega XRCs indicates that there is an anisotropic character in crystal quality in addition to the anisotropic character in surface morphology. The smaller FWHM for the $\phi=0^\circ$ than that for the $\phi=90^\circ$ indicates that less mosaic exists along the $[0001]$ direction. In comparison with recent report that c -plane ZnO thin film grown on c -plane sapphire by Zhang *et al.* [24], our results revealed a -plane ZnO possessed higher crystal quality and shown a better rough surface morphology. The prevailing cause is due to small mismatch grown on the r -plane sapphire by inserting a -plane GaN as buffer layer. As the lattice mismatch is concerned, the in-plane lattice period of ZnO along the $[\bar{1}\bar{1}00]$ direction is $\sqrt{3} a_{\text{ZnO}} = 0.5629$ nm, while the one of the GaN $[\bar{1}\bar{1}00]$ direction is $\sqrt{3} a_{\text{GaN}} = 0.5524$ nm. Therefore, the lattice mismatch could be calculated as 1.9%. On the other hand, the lattice period of ZnO along

the [0001] direction is $c_{\text{ZnO}} = 0.5207$ nm, while the one of the GaN [0001] is $c_{\text{GaN}} = 0.5185$ nm. Thus, the lattice misfit is as small as 0.4% which is a good approach of the lattice constant. Both misfits along in-plane [0001] and $[\bar{1}\bar{1}00]$ directions are much smaller than a -plane ZnO directly grown on the r -plane sapphire, which is 1.51% (18.31%) parallel (perpendicular) to the axis of the [0001] direction, without inserting the a -plane GaN as buffer layer. For this reason, ZnO film directly deposited on the underneath GaN film is nearly lattice match growth. The different values of the misfit could be used to explain the larger FWHM for the $\phi = 90^\circ$ might be related with the larger lattice misfit along the $[\bar{1}\bar{1}00]_{\text{ZnO}}//[\bar{1}\bar{1}00]_{\text{GaN}}$ direction. Additionally, the values measured from XRC indicates the good crystalline quality of non-polar ZnO film, one prevailing cause of which might be small misfit grown on the underneath GaN. Another consideration might be taken about the thickness of the film. The FWHM from XRC of crystalline quality might decrease with increasing thickness of the film, which results in stress release in the film. Thus, 3.39 μm thickness of the non-polar ZnO film resulting in a relaxation of the misfit might be another reason of good crystalline quality.

Optical property of non-polar ZnO film was measured by PL measurement with pumping wavelength 325nm of He-Cd laser. Fig. 3-2-7 demonstrates the room temperature PL spectrum. The appearance of a single strong, dominated and high-intensity emission

wavelength of 383 nm in UV region was observed in the film. The UV emission is also called near band edge emission and originated by the recombination of the free excitons at room temperature, while the wide green band (500nm~600nm) in the visible region, known as deep level emission, is generally explained by the recombination of the photo-generated holes and the electrons which belong to the singly ionized oxygen vacancies [26]. This is, the oxygen vacancies were reduced while the nanograss structure transitioned to the film. One of the vital aspects of the optical characterization of non-polar ZnO film is the intensity ratio $I_{UV} : I_{DL}$ between the UV emission and the so-called green band. As the aspects of nanograss and nanosprout structure, domination of the green level emission implies awful material properties. For film structure, the near band edge emission dominates over the green level emission and an $I_{UV} : I_{DL}$ ratio is 7:1 at room temperature. It has been known that if the crystal quality improves, for instance, the deposited structures show less structural defects and low impurity contents (less oxygen vacancies, less zinc interstitials, etc.), the PL spectra shows a sharp and strong UV emission and a suppressed and weak green emission [27]. The reason for obtaining a good quality might be speculated on the long-time growth of the non-polar ZnO film, which leads to the decrease of oxygen vacancies because oxygen gas was long-time supplied oxygen atoms to repair the oxygen vacancy sites. Therefore, the presence of a strong UV emission and weak green emission from the non-polar ZnO film indicated that the film have good crystal quality with less structural defects and exhibit



excellent optical properties.

Temperature-dependent PL spectra of non-polar ZnO film were recorded between 20 and 300 K, as shown in Fig. 3-2-8. At 20K, one of the emission lines at 3.36 eV is assigned to the recombination of a neutral donor-bound exciton ($D^{\circ}X$) and another emission line at 3.32 eV is identified to a neutral acceptor-bound exciton ($A^{\circ}X$) [27]. The FWHMs of the $D^{\circ}X$ and $A^{\circ}X$ line at 20K was measured to be 28 and 20 meV, respectively : this is a good result because the lattice mismatch between ZnO and GaN remains small. As the temperature increased, the donor-bound exciton and acceptor-bound exciton decreased in energy and merged because of the thermal ionization of the excitons and the presence of thermally activated non-radiative recombination mechanisms. For the temperature $> 220K$, the PL spectra were merged into a single UV band. In order to approach its nature, the thermal quenching of the PL integrated intensity of the UV band was studied.

The PL intensity of the donor-bound excitons and acceptor-bound excitons in the non-polar ZnO film as a function of temperature exhibits a variation at about 80 K. One can also see that the PL intensity of the donor-bound excitons represents a negative thermal quenching. To explain the origin of these effects, we analyzed the integral PL intensity in the UV region. The integral PL intensity usually decreasing with raising temperature can be described by the following formula :

$$I(T) = \frac{I_0}{1 + A \exp\left(-\frac{E_{a1}}{k_B T}\right) + B \exp\left(-\frac{E_{a2}}{k_B T}\right)} \quad \text{Eq. 3-2-1}$$

, where I_0 is the peak intensity at temperature $T = 0$ K, A and B are parameters, E_{a1} and E_{a2} are the activation energies in the thermal quenching process, and k_B is the Boltzmann constant. The advantage of having a large exciton binding energy for some device applications is clearly seen from Eq. 3-2-1. Indeed, the PL intensity increases almost exponentially with the activation (binding or localization) energy at a given temperature.

Fig. 3-2-9 demonstrates the integral PL intensity calculated in the UV region of energies as a function of the inverse temperature for non-polar ZnO film. The curve in Fig. 3-2-9 represents the results of the best fit according to Eq. 3-2-1. In the case of non-polar ZnO film, the activation energy of D⁰X is found to be 9 meV for $T < 80$ K and 53 meV for $T > 80$ K.

These activation energies reflect very well the properties of PL spectra in Fig. 3-2-8.

Namely, for $T < 80$ K the PL originates from the recombination of the donor-bound excitons with the localization energy of ~ 9 meV: $(D, X) \rightarrow D + X$, while for $T > 80$ K the PL originates from the recombination of the free exciton with the binding energy of about 53 meV. The mechanism of the negative thermal quenching is the thermal activation of carriers with energies smaller than those of the initial state of PL emission [28]. For the temperatures above 120 K, the activated acceptor levels supply charge carriers for the

observed donor-bound exciton recombination at higher energies, which can explain the increase of the donor-bound exciton PL intensity with the temperature observed in Fig. 3-2-8. In the case of the acceptor-bound exciton, the activation energy is found to be 9.2 meV for $T < 80\text{K}$, while it is 39 meV for $T > 80\text{K}$. It is determined that for $T < 80\text{K}$ PL can originate from either the acceptor-bound exciton emission or recombination of the donor-acceptor pairs, where the observed activation energy could be explained by a transition between the acceptor-bound exciton and the donor-acceptor pair energy levels. On the other hand, for $T > 80\text{K}$ the acceptor-bound exciton has the activation energy of 39 meV, which is approximately equal to the difference between donor-bound and acceptor-bound exciton energies. It means that in this temperature region, PL is due to the recombination of the acceptor-bound excitons and the activation energy is due to the re-localization (donor-bound to acceptor-bound) of the exciton. The peak positions of the observed excitonic emission lines are plotted against temperature in Fig. 3-2-10. Due to the temperature-induced change of lattice parameters and electron-lattice interaction, the excitonic emission energy follows the well-known Varshni equation :

$$E(T) = E(0) - \frac{\alpha T^2}{T + \beta} \quad \text{Eq. 3-2-2}$$

, where α , β , and $E(0)$ are fitting parameters. The obtained α and β values are $(8.2 \pm 0.4) \times 10^{-4}$

eV/K and 900(\pm 30)K for the two emission lines. $E(0)$ is 3.368 eV for donor-bound exciton emission and 3.316 eV for acceptor-bound exciton emission. The calculated temperature dependence is demonstrated by solid curves and well fits the experimental values. The red-shifted donor-bound and acceptor-bound excitons support their excitonic transitions.

3-2-3 Summary

In conclusion, we reported the fabrication of non-polar ZnO film on r -plane sapphire via inserting a -plane GaN buffer layer by using thermal vapor deposition. The thickness of non-polar ZnO film was 3.39 μm . The surface of non-polar ZnO was analyzed by AFM. The parallel [0001] direction stripes on the ZnO surface were observed, which is due to the growth rate along c -direction was faster than m -direction. In addition, the root mean square roughness of non-polar a -plane ZnO is 12.9 nm. ($11\bar{2}0$)-oriented crystal phase was confirmed by XRD θ - 2θ scan and the good quality of non-polar ZnO film was obtained by rocking curve. The FWHMs of XRC for the ($11\bar{2}0$)-oriented ZnO film were about 915 arcsec with $\phi=0^\circ$ and 1180 arcsec with $\phi=90^\circ$, which were parallel and perpendicular to [0001] direction. The cause is probably due to small misfit by inserting the 2 μm a -plane GaN film as buffer layer to reduce the lattice mismatch between ZnO and r -plane sapphire. PL measurement exhibited a sharp near band edge emission at 383 nm and an unapparent green luminescence induced by deep level emission at room temperature. Furthermore,

temperature-dependent PL spectra indicated the neutral donor-bound exciton and acceptor-bound exciton could gradually transit to FX with increasing temperature. Subsequently, activation energies of $D^{\circ}X$ and $A^{\circ}X$ were found to be 9 meV and 9.2 meV for $T < 80K$ and 53 meV and 39 meV for $T > 80K$, respectively. Finally, such non-polar ZnO films should have great potential for applications of novel optoelectronic devices and nano-photonics due to this suitable fabrication process.

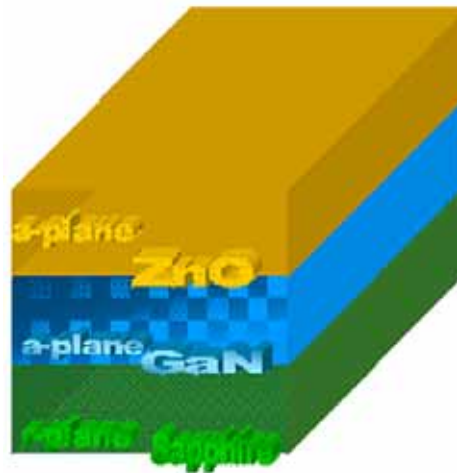


Fig. 3-2-1 Schematic drawing of growing non-polar ZnO on *r*-plane sapphire via inserting *a*-plane GaN as buffer layer.

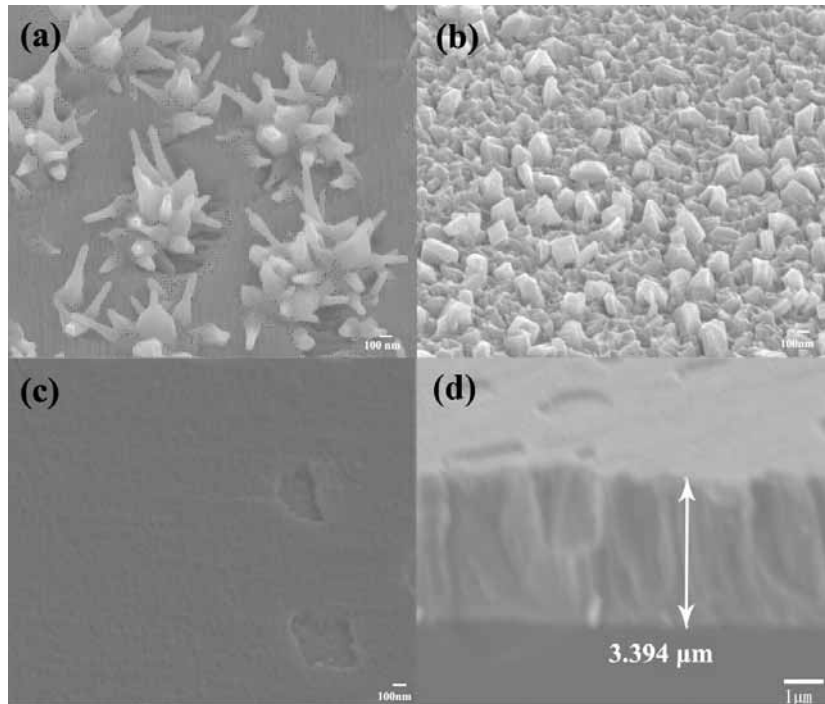


Fig. 3-2-2 The surface SEM images of non-polar ZnO grown on *r*-plane sapphire via inserting *a*-plane GaN as buffer layer at the temperature of (a) 700°C、(b) 800°C and (c) 900°C. (d)The cross-section SEM image indicates the thickness of the film is 3.39μm.

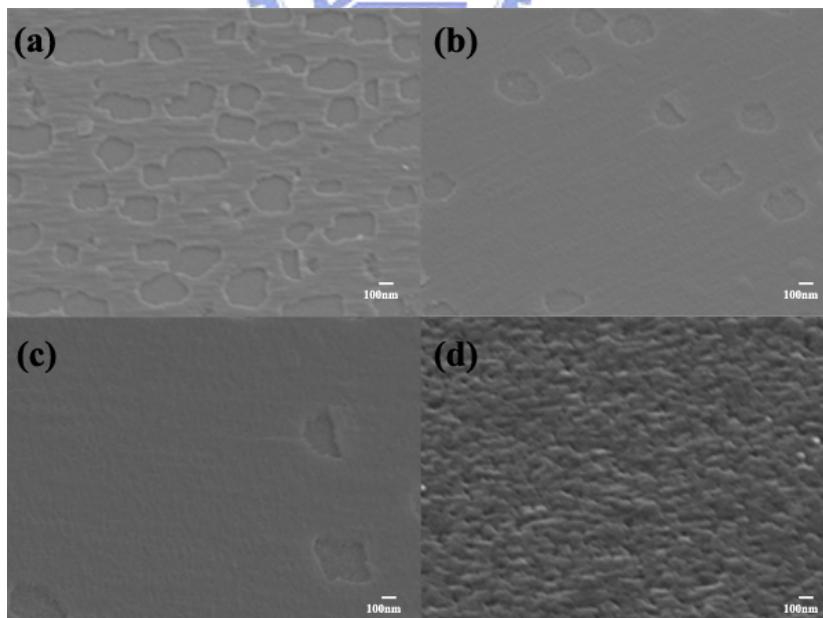


Fig. 3-2-3 The surface SEM images of non-polar ZnO grown on *r*-plane sapphire via inserting *a*-plane GaN as buffer layer at the temperature of 900°C with growth period of (a) 6 hours, (b)7 hours, (c)8 hours, and (d)9 hours.

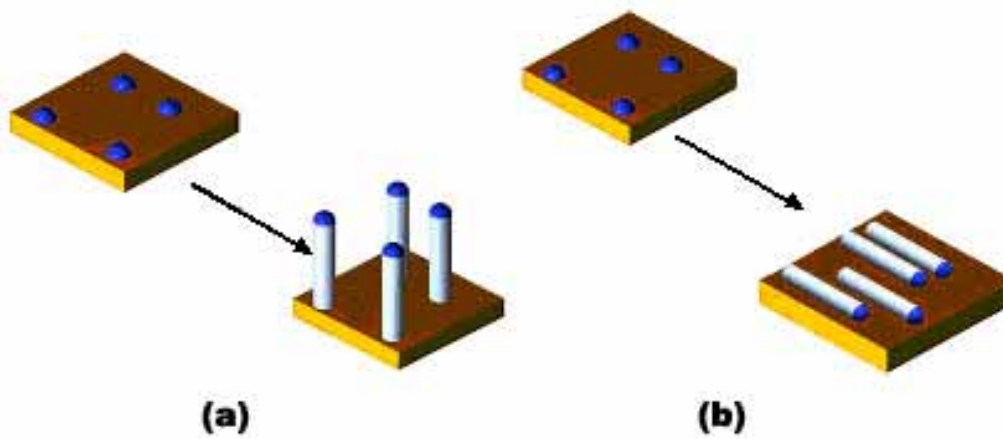


Fig. 3-2-4 Schematic growth mechanism by using thermal vapor deposition on (a) *c*-plane and (b) *a*-plane substrate

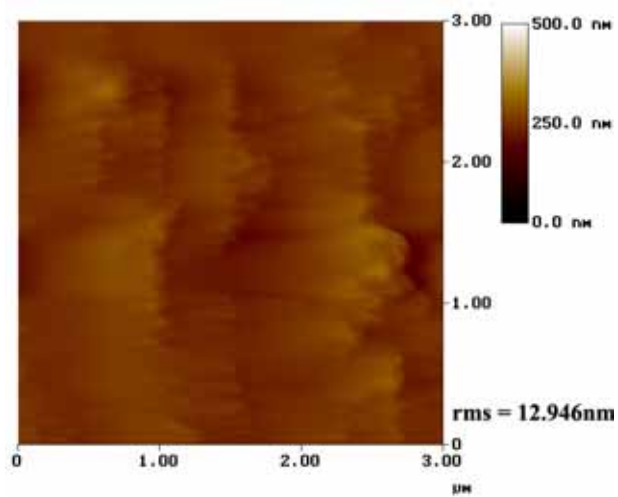


Fig. 3-2-5 The surface AFM image of non-polar ZnO film. The RMS is 12.9nm.

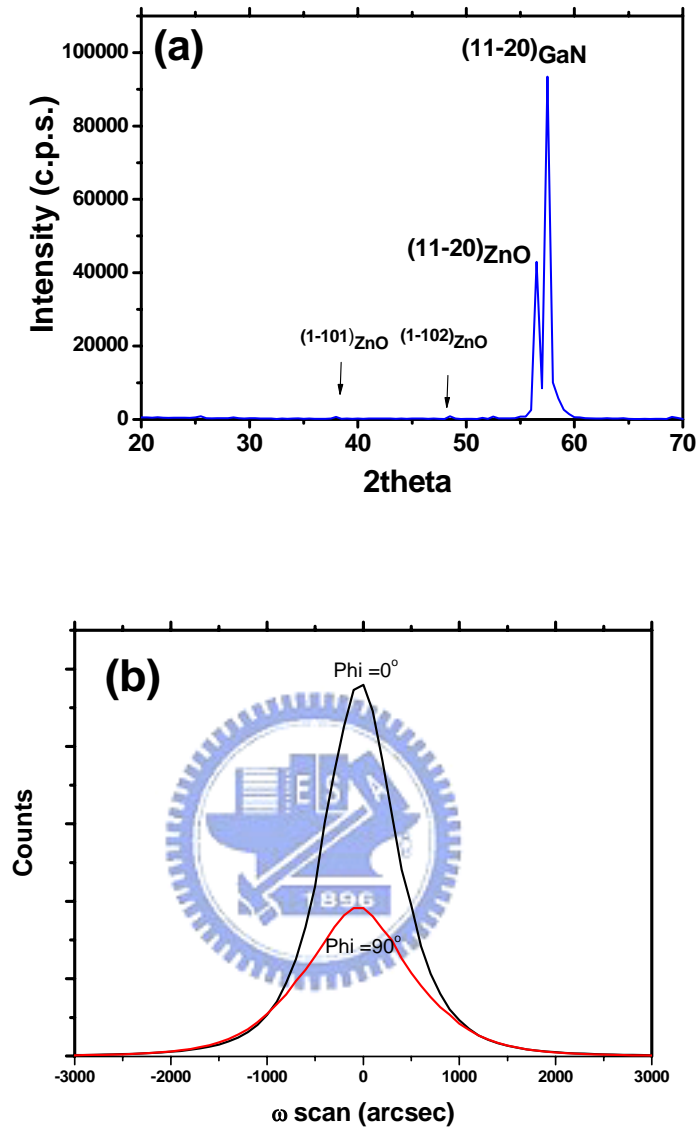


Fig. 3-2-6 (a) the θ - 2θ scan and (b) the rocking curve XRD pattern of the non-polar ZnO film. The $\varphi = 0^\circ$ (90°) represent that the (0001) direction of the ZnO is parallel (perpendicular) to the X-ray beam.

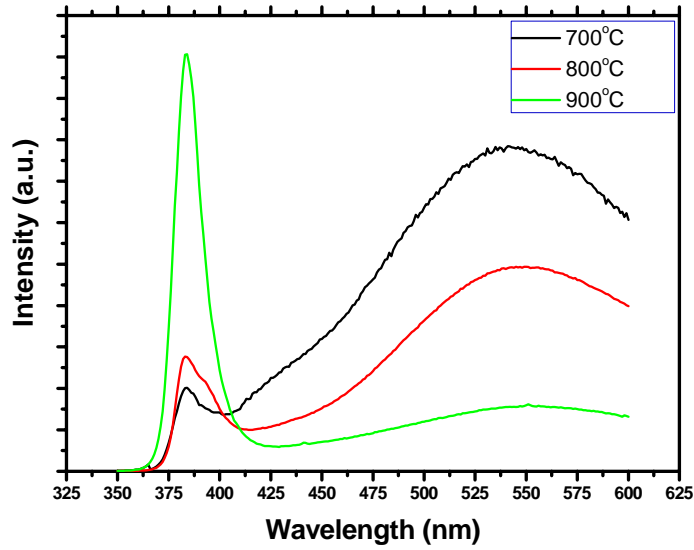


Fig. 3-2-7 Room temperature PL spectrum of ZnO at the growth temperature of 700°C, 800°C, and 900°C grown on *r*-plane sapphire via inserting *a*-plane GaN as buffer layer.

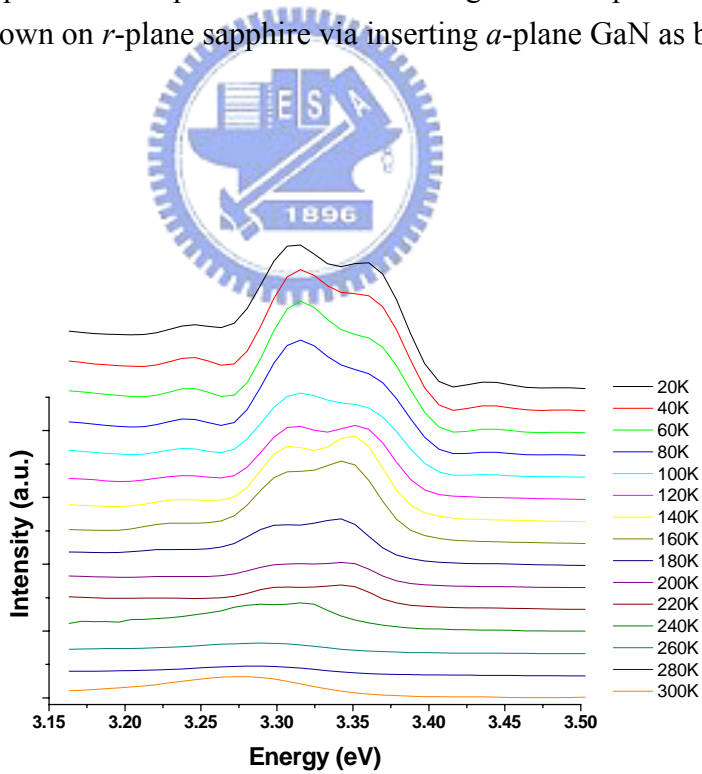


Fig. 3-2-8 Temperature-dependent PL analysis of *a*-plane ZnO. The neutral donor-bound exciton and acceptor-bound exciton were observed at low temperature.

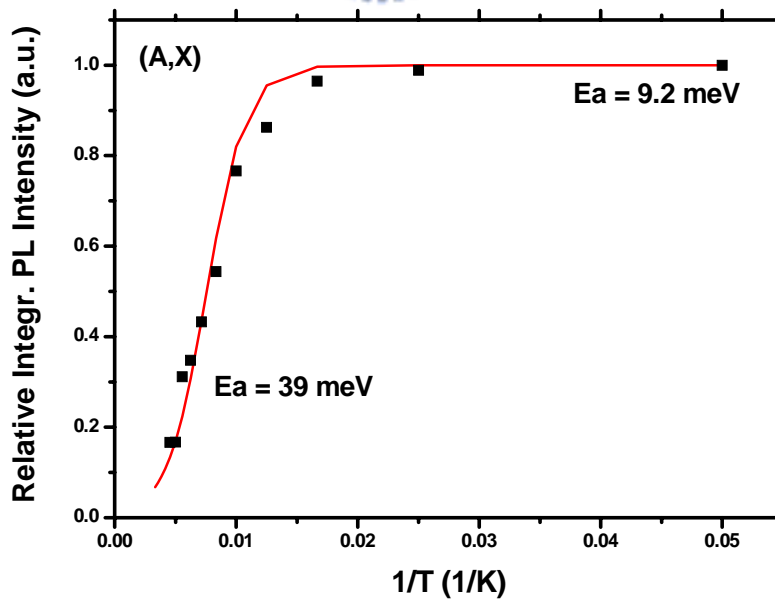
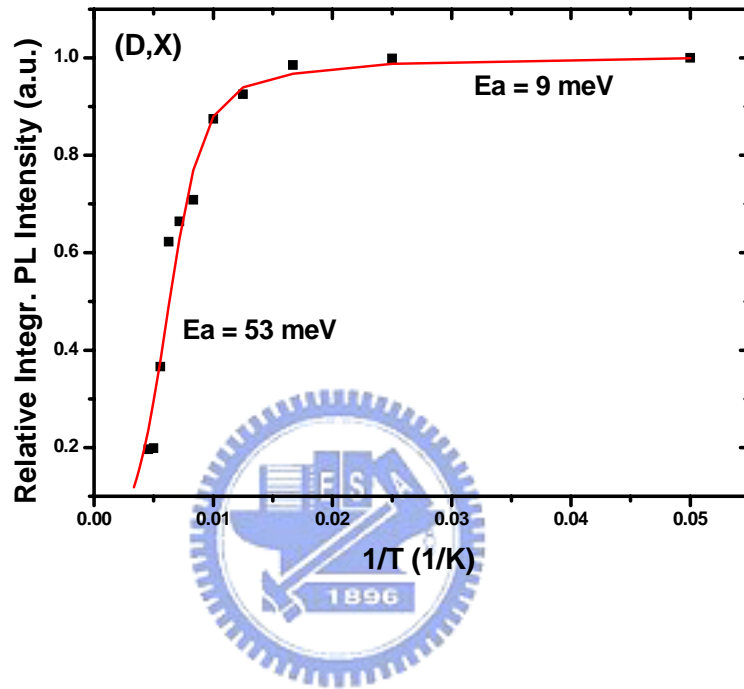


Fig. 3-2-9 The calculation of the activation energy of donor-bound exciton and acceptor-bound exciton from the temperature-dependent PL.

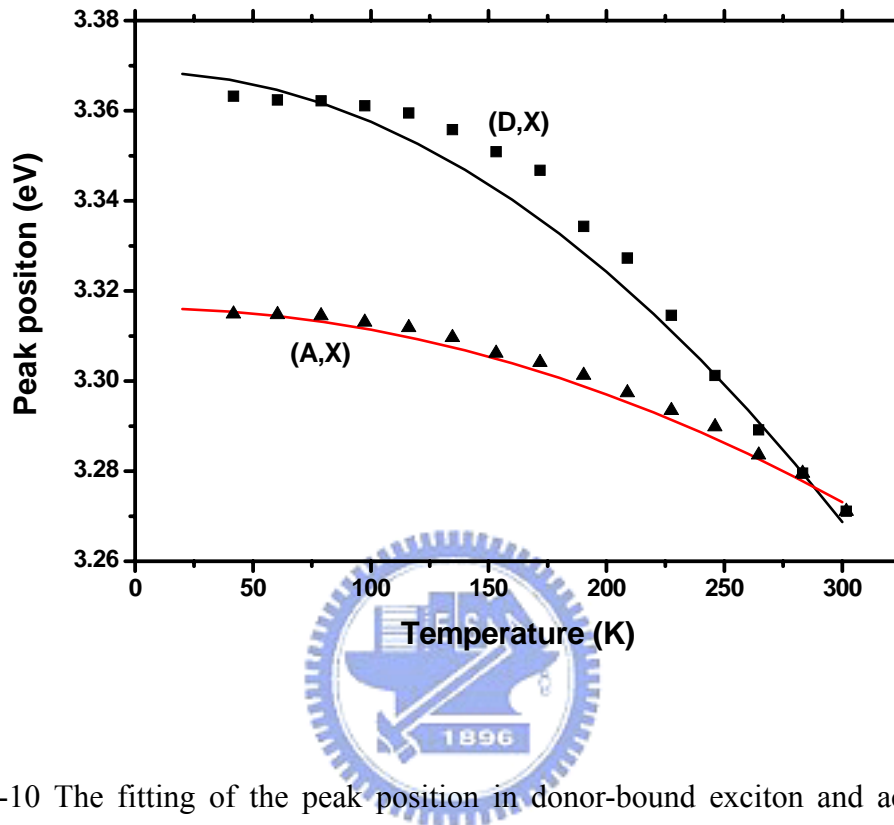


Fig. 3-2-10 The fitting of the peak position in donor-bound exciton and acceptor-bound exciton with increasing temperature according to Varshni law.

Chapter 4 Conclusion

We have successfully found a simple method to improve the quality of non-polar *a*-plane Gallium Nitride and to fabricate the high quality of non-polar Zinc Oxide by using thermal vapor deposition method in two-zone reactor. Apparently, the improvement of non-polar *a*-plane Gallium Nitride and the growth of non-polar Zinc Oxide have paved the way for well-performed UV light source application in the subsequent epitaxy.

In the first part of the thesis, the crystal quality improvement of *a*-plane GaN grown on *r*-plane sapphire was by means of thermal annealing on as-grown samples in nitrogen ambient. The best surface morphology was discovered at the annealing temperature of 1000 °C and the RMS value is 0.4 nm. The defects, such as threading dislocation and stacking fault, were decreased at the 1000 °C -annealed *a*-plane GaN. Optical property of the 1000 °C -annealed *a*-plane GaN also have good enhancement of the near band edge emission. Owing to the reduction of the non-radiative recombination centers, the quenching of the deep level emission was observed. By using a simple thermal annealing process, a smooth surface and less defect density in annealed *a*-plane GaN grown on *r*-plane sapphire could be beneficial to various optoelectronic device applications.

In the second part of the thesis, non-polar ZnO film was grown on *r*-plane sapphire via

inserting *a*-plane GaN layer as buffer layer by using furnace. The best RMS of our experiments is 12.9 nm, which still have more efforts to become smoother. Good crystal quality was confirmed by XRC and optical property. PL measurement exhibited a sharp near band edge emission at 383 nm and an unapparent green luminescence induced by deep level emission at room temperature. Furthermore, temperature-dependent PL spectra indicated the neutral donor-bound exciton and acceptor-bound exciton could gradually transit to FX with increasing temperature. Subsequently, activation energies of D⁰X and A⁰X were found to be 9 meV and 9.2meV for T<80K and 53 meV and 39meV for T>80K, respectively.



Chapter 5 Future work and prospect

As the mention above, Zinc Oxide is a very attractive candidate for blue-ultraviolet lasers operating at room temperature owing to its remarkable exciton binding energy (60meV) and oscillator strength. It implies more excitons exist within the Zinc Oxide in the room temperature and lead to larger luminescence. If Zinc Oxide is grown as a cavity with top- and bottom- distributed Bragg reflector (DBR), polaritons within the strong coupling regime might be observed in the room temperature, even larger Rabi splitting. Therefore, in the future work, I will dedicate myself to the bulk ZnO-based hybrid microcavities with $\text{Al}_{0.2}\text{Ga}_{0.8}\text{N}/\text{AlN}$ DBR at the bottom and $\text{SiO}_2/\text{HfO}_2$ DBR at the top mirror. With the careful design and accurate growth, polariton dispersion curve might be acquired and Rabi splitting might be estimated. In the further study, ZnO-based microcavities can be used to realize polariton lasers.

Reference

- [1] T. Takeichi, S. Sota, M. Katsuragawa, M. Komori, H. Takeuchi, H. Amano, I. Akasaki, *Jpn. J. Appl. Phys. Part* **236**, L382 (1997)
- [2] M.D. Craven, P. Waltereit, J. S. Speck, and S. P. DenBaars, *Appl. Phys. Lett.* **84**, 496 (2004)
- [3] Feng Wu, Michael D. Craven, Sung-Hwan Lim, and James S. Speck, *J. Appl. Phys.* **94**, 942 (2003)
- [4] U. Ozgur, Ya. I. Alivov, C. Liu, A. Teke, M. A. Reshchikov, S. Dogan, V. Avrutin, S.-J. Cho, and H. Morkoc, *J. Appl. Phys.* **98**, 041301 (2005)
- [5] Jujie Zhu, A. Yu. Kuznetsov, Myung-Soo Han, Young-Sik Park, Haeng-Keun Ahn, Jin-Woo Ju, and In-Hwan Lee, *Appl. Phys. Lett.* **90**, 211909 (2007)
- [6] A. V. Rodina, M. Strassburg, M. Dworzak, U. Haboeck, A. Hoffmann, A. Zeuner, H. R. Alves, D.M. Hofmann, and B.K. Meyer, *Phys. Rev. B* **69**, 125206 (2004)
- [7] Woo-Jin Lee, Joongoo Kang, and K. J. Chang, *Phys. Rev. B* **73**, 024117 (2006)
- [8] A. Krtschil, A. Dadgar, N. Olernik, J. Blasing, A. Diez, and A. Krost, *Appl. Phys. Lett.* **87**, 262105 (2005)
- [9] K. Domen, K. Horino, A. Kuramata, and T. Tanahashi, *Appl. Phys. Lett.* **71**, 1996 (1997)
- [10] M.D. Craven, S. H. Lim, F. Wu, J.S. Speck, and S. P. Denbaars, *Appl. Phys. Lett.* **81**, 469 (2002)
- [11] Arpan Chakraborty, K. C. Kim, F. Wu, J. S. Speck, S. P. DenBaars, and U. K. Mishra, *Appl. Phys. Lett.* **89**, 041903 (2006)
- [12] M. Asif Khan, Q. Chen, R. A. Skogman, and J. N. Kuznia, *Appl. Phys. Lett.* **66**, 2046

(1995)

- [13] J. C. Zolper, M. H. Crawford, A. J. Howard, J. Ramer, and S. D. Hersee, *Appl. Phys. Lett.* **68**, 200 (1996)
- [14] J. M. Hayes, M. Kuball, A. Bell, I. Harrison, D. Korakakis, and C. T. Foxon, *Appl. Phys. Lett.* **75**, 2097 (1999)
- [15] Z. T. Chen, K. Xu, L. P. Guo, Z. J. Yang, Y. Y. Su, X. L. Yang, Y. B. Pan, B. Shen, H. Zhang, and G. Y. Zhang, *J. Cryst. Growth* **294**, 156 (2006) thermal improve
- [16] R. Groh, G. Gerey, L. Bartha, and J. I. Pankove, *Phys. Stat. Sol. (a)* **26**, 353 (2006).
- [17] P. Vennéguès and Z. Bougrioua, *Appl. Phys. Lett.* **89**, 111915, (2006).
- [18] H. Xiao, *Introduction to Semiconductor Manufacturing Technology*, Upper Saddle River, New Jersey, Prentice Hall Inc., 2001.
- [19] J. F. Yan, L. W. Guo, J. Zhang, X. L. Zhu, G. J. Ding, Z. G. Xing, Z. T. Zhou, X. J. Pei, Y. Wang, H. Q. Jia, H. Chen, and J. M. Zhou, *J. Cryst. Growth* **307**, 35 (2007).
- [20] Jeong Ho Ryu, Dong Keun Oh, Seon Tae Yoon, Bong Geun Choi, Jong-Won Yoon, and Kwang Bo Shim, *J. Cryst. Growth* **292**, 206(2007)
- [21] For a review, see S.C. Jain, M. Willander, J. Narayan, R.V. Overstraeten, *J. Appl. Phys.* **87** (2000) 965
- [22] J. M. Hayes, M.Kuball, A bell, I. Harrison, D. Korakakis, and C. T. Foxon, *Appl. Phys. Lett.* **75**, 2097 (1999)
- [23] P. W. Tasker, *J. Phys. C* **12**, 4977 (1979)
- [24] B. P. Zhang, K. Wakatsuki, N. T. Binh, N. Usami, Y. Segawa, *Thin Solid Films* **449**, 12(2004)
- [25] H. M. Cheng, H. C. Hsu, Y.K. Tseng, L.J. Lin, W.F. Hsieh, *J. Phys. Chem. B* **109**, 8749(2005)

- [26] K. Vanheusden, C.H. Seager, W.L. Warren, D.R. Tallant, J.A. Voigt, *J. Appl. Phys.* **79**,7983 (1996)
- [27] Vladimir A. Fonoberov, Khan A. Alim, and Alexander A. Balandin, *Phys. Rev. B* **73**, 165317 (2006)
- [28] H. Shibata, *Jpn. J. Appl. Phys.*, **37**, 550 (1998)
- [29] A.V.Rdina, M.Strassburg, M.Dworzak, U.Haboeck, and A. Hoffmann, *Phys. Rev. B* **69**, 125206 (2004)
- [30] D. Reynolds, D. Look, B. Jogai, C. Litton, G. Cantwell, and W. Harsch, *Phys. Rev. B* **60**, 2340 (1999)
- [31] S.F. Chichibu, T.Sota, G.Cantwell, D.B. Eason, and C.W. Litton, *J. Appl. Phys.* **93**, 756(2003)
- [32] S.K. Han, S.K. Hong, J.W. Lee, J.Y. Lee, J.H. Song, Y.S. Nam, S.K. Chang, T. Minegishi, T. Yao, *J. Cryst. Growth* **309**, 121 (2007)
- [33] S. Ghosh, P. Waltereit, O. Brandt, H.T. Grahn, and K.H.Ploog, *Phys. Rev. B* **65**, 075202 (2002)
- [34] Bernard Gil, *Phys. Rev. B* **64**, 201310 (2001)
- [35] M. A. Reshchikov, P. Visconti, and H. Morkoc, *Appl. Phys. Lett.* **78**, 177 (2001)